Data-driven exploration and continuum modeling of dislocation networks

Markus Sudmanns[1], Jakob Bach[2], Daniel Weygand[1], Katrin Schulz[1]

E-mail: katrin.schulz@kit.edu

[1]Institute for Applied Materials, Karlsruhe Institute of Technology, Kaiserstraße 12, 76131 Karlsruhe, Germany
[2]Institute for Program Structures and Data Organization, Karlsruhe Institute of Technology, Kaiserstraße 12, 76131 Karlsruhe, Germany

Abstract.

The microstructural origin of strain hardening during plastic deformation in stage II deformation of face-centered cubic (fcc) metals can be attributed to the increase in dislocation density resulting in a formation of dislocation networks. Although this is well a known relation, the complexity of dislocation multiplication processes and details about the formation of dislocation networks have recently been revealed by discrete dislocation dynamics (DDD) simulations. It has been observed that dislocations, after being generated by multiplication mechanisms, show a limited expansion within their slip plane before they get trapped in the network by dislocation reactions. This mechanism involves multiple slip systems and results in a heterogeneous dislocation network, which is not reflected in most dislocation-based continuum models. We approach the continuum modeling of dislocation networks by using data science methods to provide a link between discrete dislocations and the continuum level. For this purpose, we identify relevant correlations that feed into a model for dislocation networks in a dislocation-based continuum theory of plasticity. As a key feature, the model combines the dislocation multiplication with the limitation of the travel distance of dislocations by formation of stable dislocation junctions. The effective mobility of the network is determined by a range of dislocation spacings which reproduces the scattering travel distances of generated dislocation as observed in DDD. The model is applied to a high-symmetry fcc loading case and compared to DDD simulations. The results show a physically meaningful microstructural evolution, where the generation of new dislocations by multiplication mechanisms is counteracted by a formation of a stable dislocation network. In conjunction with DDD, we observe a steady state interplay of the different mechanisms.

Keywords: Crystal plasticity, Continuum dislocation dynamics, Dislocation networks, Data science, Data-driven modeling

1. Introduction

Dislocation networks interconnecting different slip systems are a key feature of stage II hardening in fcc single crystals which have been observed and described in early experimental works [1, 2, 3]. Recent discrete dislocation dynamics (DDD) investigations allow for a deeper understanding of the microstructural features which govern the effective mobility of dislocations in networks [4]. It has been shown that dislocation multiplication mechanisms lead to cascades of further reactions and multiplication events, which can span the whole simulation volume even though the multiplication events are local. In the course of this observation, a dislocation may trigger several other reactions but its own travel distance is limited by the reaction it triggers. The consequence is the formation of a dense and relatively stable dislocation network. Within the network, a large scatter in dislocation spacings and travel distances of individual dislocations is observed [4, 5]. Thus, dislocation networks are characterized by individual and very heterogeneous dislocation reaction and multiplication events.

Some existing models, e.g. [6, 7], approach the challenge of modeling dislocation-based plasticity in the stage II hardening regime by phenomenological formulations based on modifications of the Kocks-Mecking formulation [8] using a 'Taylor'-like mobility law [9] to capture strain hardening. Other models account for *immobile* dislocation density, which either incorporates forest interaction as presented e.g. in [10, 11, 12], or the formation of dislocation dipoles, e.g. in [13, 14]. An often used *kinematic* formulation of dislocation dynamics is based on [15] which describes connected edge and screw dislocations, where the motion of one dislocation type increases the line length of the other type. However, most existing approaches combine all mechanisms into slip-system-wise formulations, usually incorporating an internal length scale which is referred to as 'mean free path' of dislocations [11, 10]. Therefore, microscopic details such as the dislocation density increase on inactive slip systems and the explicit coupling of several slip systems by dislocation reactions are not reflected. Moreover, despite the usual interpretation of the 'Taylor' relation as the critical shear stress to move 'pinned' dislocation segments [16, 17], statistical variation of segment lengths in dislocation networks have not received much attention in existing continuum models.

In order to reflect the dislocation dynamics in dislocation networks, we aim for a clear separation of the dislocation line length increase, resulting in plastic slip, from the mechanisms which govern the *rate* of the plastic slip. In contrast to the edge-screw approaches mentioned above, the Continuum Dislocation Dynamics (CDD) theory [18, 19, 20] formulates the kinematic properties of curved dislocation lines. This is achieved by incorporating the so-called *curvature density* additionally to the dislocation density, where the former represents the change in dislocation curvature along the dislocation line. Since the integral of the curvature density can be interpreted as the number of dislocations, the CDD theory allows for the explicit consideration of mechanisms which separately address the dislocation line, whose length is represented by the dislocation density, and the dislocation as a closed object. This separation

provides the basis for the formulation of dislocation multiplication by glissile reactions and cross-slip in [21], which is a first step towards a physically based formulation of dislocation networks in a dislocation based continuum theory. However, in order to reflect further details of dislocation network evolution, the presented model in [21] still needs an incorporation of dislocation mechanisms which stabilize the dislocation network and curvature density, which is 'stored' in end-nodes of dislocation junctions. Further, a concept of how to approach the statistical variance in dislocation spacings and travel distances still has to be developed.

We present a model of dislocation network formation based on physically inspired formulations for the evolution of dislocation reactions while maintaining the kinematic description of dislocation expansion and plastic strain evolution based on single slip systems. Using data-driven methods for the analysis of DDD networks and systematic feature selection to identify physically meaningful correlations, continuum terms are derived to represent dislocation reactions during the network evolution. By extending the model of dislocation multiplication presented in [21], we formulate evolution equations for dislocation reactions leading to sessile dislocation junctions (Lomer reaction) and junctions of zero Burgers vector (collinear reaction). The proposed continuum model accounts for two competing mechanisms: (i) the generation of *new* dislocations, which allows for further plasticity and (ii) the limitation of the dislocation mobility, i.e. the limitation of the plasticity generated by each individual dislocation. Thus, the model averages the dislocation reaction cascades observed in DDD into a slip rate, which is modified by *source* and *sink* terms for the dislocation density and curvature density evolution. The interplay of the different mechanisms is analyzed in a simple system followed by a comparison of the model to DDD simulations [4]. As a result, dislocation network formation is achieved by explicit consideration of the evolution of dislocation reactions - through their formation and dissolution - rather than generalizing the mean dislocation distance as the dominant dislocation-mobility criterion for describing the properties of dislocation networks.

2. Voxel-based analysis of dislocation networks

The strain hardening in stage II deformation of face-centered cubic (fcc) crystals is largely determined by effects originating from the intersection of dislocation lines on different slip systems, which leads to the formation of dislocation networks. According to DDD observations in [4, 5], the most important mechanisms which govern the dislocation microstructure in such networks include cross-slip as well as glissile, Lomer and collinear reactions. Based on the 3d-DDD dislocation structure investigated in [4], we consider a tensile test using a fcc single crystal with a volume of $(5\,\mu\mathrm{m})^3$. The system is subjected to a constant strain rate of $\dot{\varepsilon} = 5000\,\mathrm{s}^{-1}$, the initial dislocation density is $\rho \approx 1.15 \times 10^{13}\mathrm{m}^{-2}$. For a detailed description of the DDD material data see [4]. With respect to a subsequent continuum consideration, we transform the DDD data, consisting of discrete dislocation lines, into voxels, which contain the continuum field

variables as used in the CDD formulation according to [20].

2.1. Preparation of the voxel data set

We subdivide the simulation domain into evenly-sized cubic voxels, as visualized by Fig. 1. We represent each voxel by characteristics extracted from the DDD data. These characteristics are continuum field variables, such as the total dislocation density ρ_{tot}, or the reaction densities. The term *reaction density* denotes the dislocation density representing the line length of the reaction in the specific voxel, i.e., the line length of glissile (ρ_{gliss}), Lomer (ρ_{Lomer}) or collinear reactions (ρ_{coll}) summarized over the slip systems. We ignore Hirth reactions, since they are only very rarely observed in the underlying DDD simulations and show hardly any contribution to strain hardening, as also observed in [5]. Further, we restrict the present investigation to mechanisms in dislocation networks which are caused by intersection of dislocation lines leading to dislocation reactions. Therefore, we do not explicitly analyze dislocation mechanisms which typically dominate in single slip conditions, such as dislocation dipole formation. We also do not choose cross-slip as a voxel characteristic in the present section, since its formation mechanism is largely different from dislocation reactions. Moreover, we do not investigate the dislocation velocity in the DDD data, since its discrete characteristic in DDD is not comparable to the homogenization of the velocity in CDD in which the velocity is a spatial variable originating from averaged stress terms (see e.g. [22]). Regarding the temporal dimension, we choose sufficiently large time intervals to average local scattering in the DDD data, resulting in a number of 22 time intervals overall. Considering the spatial and temporal dimensions, we get 2750 data objects. However, the actual number of voxels used in our investigation is lower and depends on the reaction type, as we exclude voxels with a reaction density of zero. The reason for this is that a reaction density of zero implies an absence of dislocation reactions from the specific type in the specific voxel within the given averaged time interval. Depending on the reaction type, the actual number of data objects thus reduces to between 91 % and 87 % of the full data set.

2.2. Exploration of the data set

In this section, we investigate the evolution of the reaction density as obtained from the data set. Fig. 2 shows the evolution of the *measured* line length of the DDD simulation stored in dislocation reactions for a discretization of five voxels along each spacial direction. We represent each voxel and time step individually, but sum over the slip systems. The plot shows a comparable increase of reaction density with the dislocation density for all reaction types. The high relative initial scatter decreases with an increasing total density. The overall increase of reaction density with dislocation density motivates our prediction models in the next section. Additionally, the coloring in Fig. 2 shows the number of dislocations per voxel and time interval. The value is determined by counting the number of closed dislocations with unique loop index within

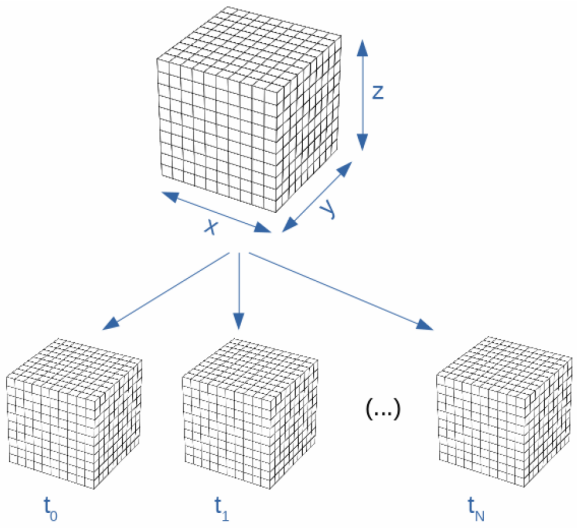

Figure 1. Subdivision of the simulation volume in voxels per time step t.

each voxel, such that one dislocation can be part of several voxels, but each loop index is only counted once in each voxel. It can be seen that the number of dislocations in each voxel also increases with increasing total dislocation density and reaction density.

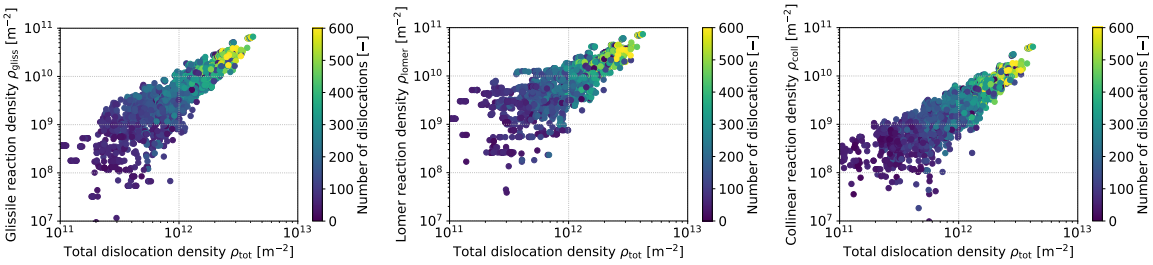

(a) Glissile reaction. (b) Lomer reaction. (c) Collinear reaction.

Figure 2. Dislocation line length per voxel volume stored in dislocation reactions (= reaction density) over total line length per voxel volume (= total dislocation density), separately for glissile (a), Lomer (b) and collinear (c) reactions. Each data point represent one voxel at one time interval and is colored according to the number of dislocations in the respective voxel.

2.3. Prediction of reaction density

Based on the findings obtained in the previous section, we want to find an adequate prediction model for the reaction densities. Considering a reaction density ρ_{react}, representing glissile, Lomer or collinear reaction density, we assume the following functional form:

$$\rho_{\text{react}} = \sum_{\xi} \sum_{\zeta} \left(\beta_1^{\xi\zeta} \rho^{\xi} \sqrt{\rho^{\zeta}} + \beta_2^{\xi\zeta} \rho^{\zeta} \sqrt{\rho^{\xi}} \right) \qquad \text{for} \qquad (\xi, \zeta) \in \pi_{\text{react}}, \tag{1}$$

where π_{react} denotes the set of all pairs of reacting slip systems for the particular reaction type. ξ and ζ are indices of the slip systems. The function relates the line length of all reactions present at a given dislocation state to the overall dislocation content and dislocation spacing on either of the coupled slip systems. Therefore, as a natural assumption for incorporating intersecting dislocation lines on two slip planes, the dislocation densities on both slip systems are coupled with the dislocation spacing on the respective forest system, which leads to the $\sqrt{\rho}$-terms. This relationship can be motivated independent of the reaction type as coupling terms of the slip system pairings π_{react}. We assume that this functional form is applicable regardless of the type of reaction, if no change in loading path is involved. As an objective of this section, we evaluate the validity of this assumption based on data-driven analyses. The reaction pairs depend on the reaction type: We have 24 reaction pairs for ρ_{gliss}, 12 reaction pairs for ρ_{Lomer} and 6 reactions pairs for ρ_{coll}, which directly originate from the fcc crystal structure. The coefficients $\beta_1^{\xi\zeta}$ and $\beta_2^{\xi\zeta}$ are unknown yet. These coefficients specify the relationship between the dislocation density on the reacting slip systems and the line length of resulting dislocation reactions.

As the equation is linear in the interaction terms, $\rho^\xi\sqrt{\rho^\zeta}$ and $\rho^\zeta\sqrt{\rho^\xi}$, we validate the equation by training and evaluating a linear regression model, separately for each reaction type. The reaction density is the prediction target and the corresponding interaction terms are the features put into the model, respectively. Before training the regression models, which we obtain from the scikit-learn library for Python, we apply min-max scaling to get all features to a common range. Furthermore, we remove features which have an absolute Pearson correlation of at least 0.95 to another feature, as linear models are known to have problems with features that are linearly related [23]. After training, we evaluate all models with the proportion of variance predicted, R^2. To determine how well our models generalize, we apply a train-test split along the temporal axis: Data from the first 17 time intervals forms the training set and data from the last 5 time intervals forms the test set.

Figure 3 compares the values predicted by the trained regression models with the ground truth values. For a discretization of five voxels along each spacial direction, we observe a high prediction quality for all three reaction types, underpinning the relationship between dislocation density and reaction density. This also shows the validity of the earlier assumption to apply the same functional form independent of the specific reaction type.

To further investigate the relationship between dislocation density and reaction density, we also explore four alternatives to Eq. (1). Since the values of $\beta_1^{\xi\zeta}$ and $\beta_2^{\xi\zeta}$ differ even within the same reaction pair, when using Eq. (1), we first use identical coefficients for each two terms in a reaction pair, i.e., $\forall\xi\ \forall\zeta\ \beta_1^{\xi\zeta} = \beta_2^{\xi\zeta}$, to analyze the impact of that simplification. Second, we simplify Eq. (1) even further by using the same coefficient for all interaction pairs:

$$\rho_{\text{react}} = \beta \sum_{\xi} \sum_{\zeta} \left(\rho^\xi \sqrt{\rho^\zeta} + \rho^\zeta \sqrt{\rho^\xi} \right) \qquad \text{for} \qquad (\xi, \zeta) \in \pi_{\text{react}}. \tag{2}$$

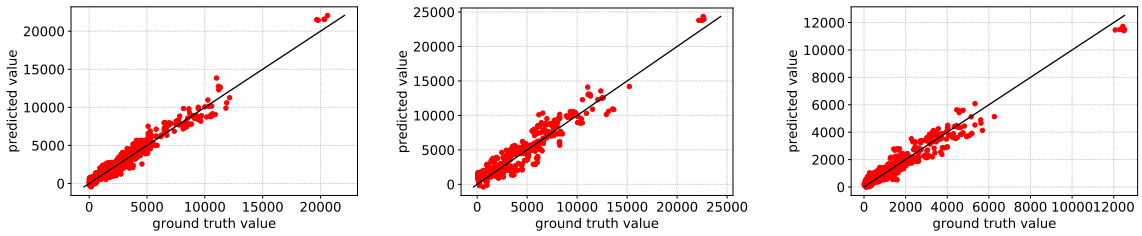

(a) Glissile reaction $R^2 = 0.954$. (b) Lomer reaction $R^2 = 0.896$. (c) Collinear reaction $R^2 = 0.937$.

Figure 3. Predicted value over ground truth of the trained model according to Eq. (1) on a mesh with $5 \times 5 \times 5$ voxels trained with multi-linear regression for glissile (a), Lomer (b) and collinear reactions (c).

Third, we combine Eq. (1) with a simple feature selection technique to get a model with only a few coefficients: For all reaction types, we sort the interaction terms according to the correlation to the prediction target, i.e. reaction density, and only choose one third or one sixth of the interaction terms with the highest correlation as features. We then train the regression model with only these features, i.e. with a limited number of interaction terms. Fourth, we use the raw dislocation densities from the 12 slip systems instead of the interaction terms. Table 1 shows the results for the predictions with the different feature sets.

Feature set	Predict ρ_{gliss}	Predict ρ_{Lomer}	Predict ρ_{coll}
Individual interaction terms (Eq. (1))	0.954 (0.956)	0.896 (0.881)	0.937 (0.936)
Eq. (1) with $\forall\xi\ \forall\zeta\ \beta_1^{\xi\zeta} = \beta_2^{\xi\zeta}$	0.952 (0.951)	0.891 (0.875)	0.937 (0.936)
All interactions terms combined (Eq. (2))	0.863 (0.881)	0.759 (0.795)	0.755 (0.774)
Eq. (1) with feature selection, k = 1/3	0.949 (0.949)	0.873 (0.863)	0.926 (0.929)
Eq. (1) with feature selection, k = 1/6	0.93 (0.931)	0.855 (0.854)	0.883 (0.905)
Dislocation densities, no interaction	0.93 (0.928)	0.879 (0.87)	0.882 (0.882)

Table 1. R^2 for predicting the reaction densities with different feature sets. The values in brackets are the results for a prediction on the training set.

We observe that setting $\beta_1^{\xi\zeta} = \beta_2^{\xi\zeta}$ does not reduce the prediction quality. In contrast, merging all interaction terms according to Eq. (2) results in a drop of prediction quality. However, as a trade-off, the number of coefficients is reduced significantly, making the model simpler. The same holds for the feature selection approach, which results in a prediction accuracy between Eq. (1) and Eq. (2). Furthermore, we can also see an accuracy decrease when increasing the feature selectivity, i.e., selecting 1/6 of the interaction terms instead of 1/3. As a simple sanity check, we also tested selecting the same number of features, but taking the features with the lowest absolute correlation to the target instead of the highest. As one could expect, prediction accuracy turned out to be clearly worse. Finally, using the raw dislocation densities without the pre-defined

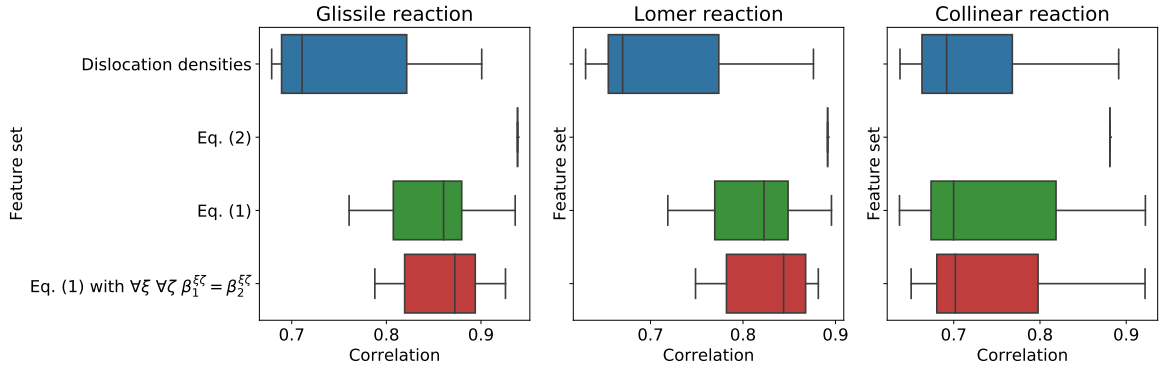

Figure 4. Correlation of different feature sets with the target variable for each reaction type, respectively.

interactions results in a similar or worse prediction performance compared to the feature sets using Eq. (1), with the largest difference for the collinear reaction density.

Figure 4 displays the correlation of features from different feature sets with the target variable, i.e. each reaction density. Here, we observe that the raw dislocation densities overall show a lower correlation with their prediction target than the interaction terms from Eq. (1). However, one needs to be aware that these correlations only analyze the relationship between each feature on its own and the target variable. In contrast, the multiple linear regression model uses a combination of all features from the corresponding feature set. This methodological difference can explain the discrepancy between correlation results and prediction results regarding the combined interaction term of Eq. (2). In this case, there is only one feature per target variable and therefore only one correlation value. We observe a high correlation with the target variable, but still obtain no better prediction quality than the individual interaction terms from Eq. (1) combined in a model.

3. Dislocation density-based continuum model

3.1. Dislocation networks in a dislocation-based crystal plasticity framework

3.1.1. Elasto-plastic framework In the continuum, we describe the elasto-plastic deformation of fcc metals by an additive decomposition of the small-strain distortion tensor into an elastic and a plastic part

$$\mathrm{D}\mathbf{u} = \boldsymbol{\beta}_{\mathrm{el}} + \boldsymbol{\beta}_{\mathrm{pl}}. \tag{3}$$

The plastic distortion, described by the tensor $\boldsymbol{\beta}_{\mathrm{pl}}$, is assumed to originate solely from the evolution of the dislocation state and is determined by evaluating the sum of the plastic slip γ^{ξ} (see section 3.1.2) over all slip systems ξ

$$\boldsymbol{\beta}_{\mathrm{pl}} = \sum_{\xi=1}^{N} \gamma^{\xi} \mathbf{d}^{\xi} \otimes \mathbf{m}^{\xi} \ . \tag{4}$$

Herein, the orientations of the slip systems are defined by the orthonormal basis $\{\mathbf{d}^\xi, \mathbf{l}^\xi, \mathbf{m}^\xi\}$ with the slip plane normal $\mathbf{m}^\xi$ and the slip direction $\mathbf{d}^\xi = \frac{1}{b}\mathbf{b}^\xi$, where $\mathbf{b}^\xi$ is the Burgers vector of length $b = |\mathbf{b}^\xi|$ and $\mathbf{l}^\xi = \mathbf{m}^\xi \times \mathbf{d}^\xi$.

Following [18, 19], the evolution of the dislocation microstructure can be described by the evolution of the total dislocation density ρ^ξ, the vector of the geometrically necessary dislocation density $\boldsymbol{\kappa}^\xi = (\kappa^\xi_{\text{screw}}, \kappa^\xi_{\text{edge}}, 0)$, and the curvature density q^ξ. The latter variable describes the local change in angular orientation of an ensemble of dislocation lines in an averaging volume. The dislocation flux-based *kinematic* evolution of the dislocation state – neglecting any change of dislocation content by dislocation reactions or cross-slip – is therefore described by the following equations, assuming an isotropic dislocation velocity v^ξ:

$$\begin{aligned}
\partial_t \rho^\xi &= -\nabla \cdot (v^\xi \boldsymbol{\kappa}^\xi_\perp) + v^\xi q^\xi \qquad \text{with} \qquad \boldsymbol{\kappa}^\xi_\perp = \boldsymbol{\kappa}^\xi \times \mathbf{m}^\xi \\
\partial_t \boldsymbol{\kappa}^\xi &= \nabla \times (\rho^\xi v^\xi \mathbf{m}^\xi) \\
\partial_t q^\xi &= -\nabla \cdot \left(\frac{q^\xi}{\rho^\xi} \boldsymbol{\kappa}^\xi_\perp v^\xi + \boldsymbol{A}^\xi \nabla v^\xi \right).
\end{aligned} \tag{5}$$

Here, we employ the closure assumptions introduced in [18] using the dislocation alignment tensor

$$\boldsymbol{A}^\xi = \frac{1}{2|\boldsymbol{\kappa}^\xi|^2} \left(\left(\rho^\xi + |\boldsymbol{\kappa}^\xi|\right) \boldsymbol{\kappa}^\xi \otimes \boldsymbol{\kappa}^\xi + \left(\rho^\xi - |\boldsymbol{\kappa}^\xi|\right) \boldsymbol{\kappa}^\xi_\perp \otimes \boldsymbol{\kappa}^\xi_\perp \right). \tag{6}$$

The relationship between shear stresses on the slip system and the dislocation velocity v^ξ is characterized by a velocity law, assuming a linear dependency between velocity and effective resolved shear stress τ^ξ. The effective resolved shear stress originates from a superposition of an external loading or boundary conditions projected on the slip plane and internal stresses of the dislocation microstructure: $\tau^\xi = \tau^\xi_{\text{ext}} + \tau^\xi_{\text{int}}$. The internal stresses represent the mean dislocation stress fields using a mean field approach as in [22] according to the numerical resolution of the system, and short range correction stresses. However, the long-range internal stress fields vanish in configurations which only consist of statistically stored dislocations (SSDs). This problem can be solved by introducing formulations for dislocation interaction and reaction, as in [14, 21] and as explained later in this section.

The elasto-plastic formulation described in this section is incorporated in the finite element code M++ based on a parallel multigrid method [24, 25], which further incorporates the numerical framework for the solution of the dislocation microstructure problem described by Eq. (5). The CDD framework is described in detail in [20]. Using a discontinuous Galerkin scheme, the equations are solved separately on each slip system. The elasto-plastic problem is solved by a standard finite element solver, where the same mesh is used for the stress computation and the evaluation of the internal variables of the microstructure.

3.1.2. Dislocation networks in the continuum Due to the planar nature of the kinematic evolution of the dislocation state in CDD (Eq. 5), any mechanism which originates from

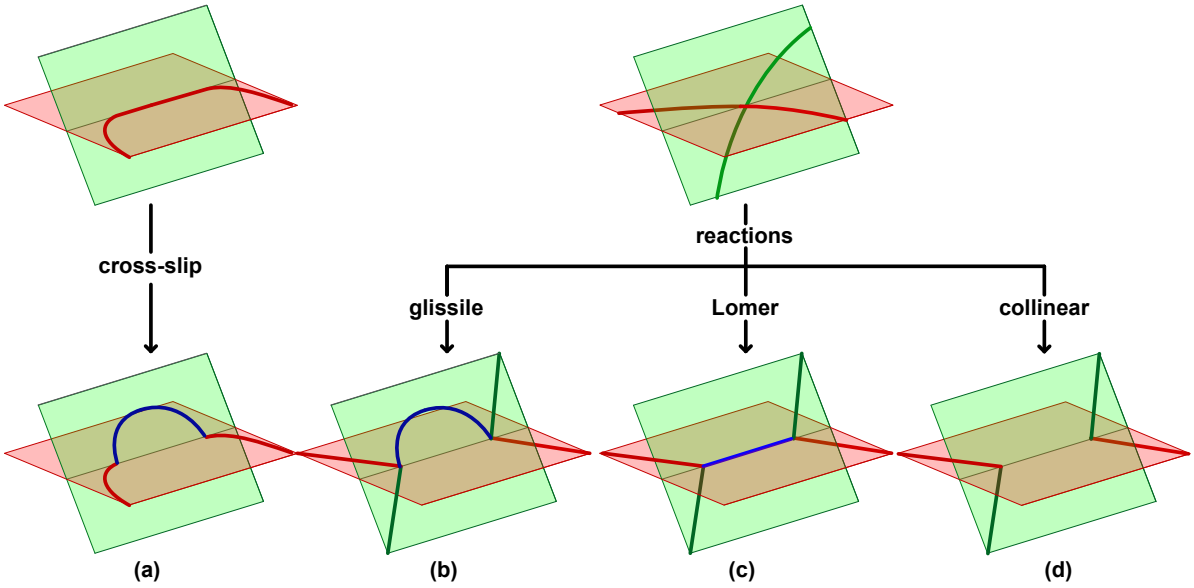

Figure 5. Schematic visualization of cross-slip (a) and occurring reactions from intersection of two dislocations showing glissile (b), Lomer (c) and collinear reactions (d).

the reaction of dislocations on different slip systems has to be included by rate equations, which modify the dislocation content as well as the curvature density on the respective slip systems. This is described in [21] for the aspect of dislocation multiplication. As for the voxel-based analysis of the DDD dislocation network in section 2, we formulate physically based evolution equations for dislocation reactions, which will be derived in detail in section 3.2 in the context of the given continuum theory. A schematic visualization of all considered mechanisms is shown in Fig. 5. Cross-slip and glissile reactions lead to dislocation multiplication by generation of new dislocations [4, 21]. In contrast, Lomer reactions lead to sessile dislocation junctions which typically impede the motion of the involved dislocations [26, 27]. The latter process is further called *stabilization* of dislocations. Collinear reactions lead to an annihilation of collinear dislocation lines sections. All reactions involve two dislocations on different slip systems, which intersect and form a dislocation reaction, as long as at least one segment is mobile.

In DDD simulations [4], it is observed that dislocations mostly do not further contribute to plastic slip once incorporated into the network e.g. by formation of dislocation reactions. Further, the network microstructure is characterized by a large scatter of the velocities and travel distances of involved dislocations. After coming into existence, generated dislocations travel only short, but very varying distances before getting caught in the network. The resulting length of dislocation lines connecting endpoints of dislocation junctions has been referred to as *link lengths*, where statistical variations of this link length have been proposed as an explanation for the emerging microstructure of dislocation networks [5, 28]. Therefore, the onset of plastic flow can be related to a 'weakest-link' argument [29]. In the context of a dislocation-based

continuum theory, we therefore incorporate a formulation in which the total dislocation density ρ^ξ is separated into a *mobile dislocation density* ρ^ξ_M, which evolves according to Eq. (5), and into a part which we call *network dislocation density* ρ^ξ_net, which does not contribute to plastic slip:

$$\rho^\xi = \rho^\xi_\mathrm{M} + \rho^\xi_\mathrm{net}. \tag{7}$$

For the rate of the plastic shear γ^ξ it thus holds

$$\partial_t \gamma^\xi = \rho^\xi_\mathrm{M} b v^\xi. \tag{8}$$

The network dislocation density ρ^ξ_net is distributed over a certain range of dislocation link lengths to capture the statistical variations in travel distances of the dislocations. This aspect will be derived in detail in section 3.2.2. The density ρ^ξ_net in Eq. (7) is further subdivided into (i) a *density of Lomer junctions* ρ^ξ_Lomer, which captures the line length of the junction between both end-nodes (visualized by the blue line in Fig. 5(c)) and (ii) a *stabilized dislocation density* ρ^ξ_S. The latter contains the line length of dislocations which are part of the stable network due to their attachment to Lomer junctions (visualized by the red and green lines in Fig. 5(c)). Both densities can be increased by the formation of Lomer junctions. This results in

$$\rho^\xi_\mathrm{net} = 0.5\rho^\xi_\mathrm{Lomer} + \rho^\xi_\mathrm{S}. \tag{9}$$

Here, the density of Lomer junctions ρ^ξ_Lomer is shared with the second involved slip system, resulting in a prefactor of 0.5. The unzipping of Lomer junctions is reproduced by a transformation of the respective fraction of the network dislocation density (ρ^ξ_net) back into mobile dislocation density, as will be derived in section 3.2.

For the evolution of the dislocation network, the network dislocation density ρ^ξ_net is defined as an internal variable, which evolves based on *sink* and *source* terms in the evolution equation of the mobile dislocation density ρ^ξ_M. The evolution of the averaged dislocation state using Eq. (5) and including cross-slip, as well as glissile, Lomer and collinear reactions results in

$$\begin{aligned}
\partial_t \rho^\xi_\mathrm{M} &= -\nabla\cdot(v^\xi\ \boldsymbol{\kappa}^\xi_\perp) + v^\xi q^\xi + \partial_t \bar{\rho}^\xi_\mathrm{M} + \partial_t \hat{\rho}^\xi_\mathrm{M} + \partial_t \bar{\rho}^\xi_\mathrm{M,Lomer} + \partial_t \rho^\xi_\mathrm{M,react} + \partial_t \rho^\xi_\mathrm{M,cross} \\
\partial_t \boldsymbol{\kappa}^\xi &= \nabla\times(\rho^\xi_\mathrm{M} v^\xi \mathbf{m}^\xi) + \partial_t \bar{\boldsymbol{\kappa}}^\xi_\mathrm{cross} \\
\partial_t \rho^\xi_\mathrm{net} &= 0.5\partial_t \rho^\xi_\mathrm{Lomer} - \partial_t \bar{\rho}^\xi_\mathrm{M,Lomer} + \partial_t \hat{\rho}^\xi_\mathrm{net} + \partial_t \rho^\xi_\mathrm{S,react} \\
\partial_t q^\xi &= -\nabla\cdot\left(\frac{q^\xi}{\rho^\xi_\mathrm{M}}\boldsymbol{\kappa}^\xi_\perp v^\xi + \mathbf{A}^\xi \nabla v^\xi\right) + \partial_t \bar{q}^\xi + \partial_t q^\xi_\mathrm{react} + \partial_t q^\xi_\mathrm{cross}.
\end{aligned} \tag{10}$$

Here, $()_\mathrm{react}$ is an index denoting different dislocation reactions, i.e. $()_\mathrm{react} = ()_\mathrm{gliss}, ()_\mathrm{Lomer}, ()_\mathrm{coll}$. Further, any process which results in the formation of a reaction is denoted by $\bar{(\ )}$, whereas the unzipping is denoted by $\hat{(\ )}$. Dislocation multiplication by cross-slip and glissile reactions leads to a generation of new dislocations which increases the *mobile density* $\partial_t \bar{\rho}^\xi_\mathrm{M} = \partial_t \bar{\rho}^\xi_\mathrm{M,gliss} + \partial_t \bar{\rho}^\xi_\mathrm{M,cross}$, the curvature density $\partial_t \bar{q}^\xi = \partial_t \bar{q}^\xi_\mathrm{gliss} + \partial_t \bar{q}^\xi_\mathrm{cross}$ and the screw-GND density $\partial_t \bar{\boldsymbol{\kappa}}^\xi_\mathrm{cross}$ in case of cross-slip. The density

of Lomer junctions is reflected by $0.5\partial_t\rho^\xi_{\text{Lomer}}$, where the reaction further transfers dislocation line length from mobile dislocation density (ρ^ξ_{M}) to its network counterpart (ρ^ξ_{net}) by $\partial_t\bar{\rho}^\xi_{\text{M,Lomer}}$. The reverse process is the *unzipping* of Lomer junctions, which *increases* the mobile density by $\partial_t\hat{\rho}^\xi_{\text{M}}$ and equally decreases the network density by $\partial_t\hat{\rho}^\xi_{\text{net}} = \partial_t\hat{\rho}^\xi_{\text{Lomer}} + \partial_t\hat{\rho}^\xi_{\text{S}}$. All dislocation reactions and cross-slip lead to a decrease of dislocation density on the reacting slip systems $\partial_t\rho^\xi_{\text{M,react}}, \partial_t\rho^\xi_{\text{M,cross}}, \partial_t\rho^\xi_{\text{S,react}}$ due to the mechanism itself. As derived in [21], we consider a concentration of dislocation curvature into the end-nodes of dislocation junctions which is reflected by $\partial_t q^\xi_{\text{react}}$ and $\partial_t q^\xi_{\text{cross}}$. Table 2 provides an overview of mechanisms, which can form mobile or network dislocation density. These mechanisms are derived in detail in section 3.2.

Mobile density is increased by		Network density is increased by	
Expansion of existing dislocations:		Formation of Lomer reactions:	
$v^\xi q^\xi$	see Eq. (5)	$0.5\partial_t\rho^\xi_{\text{Lomer}}, -\partial_t\rho^\xi_{\text{M,Lomer}}$	see Eqs. (16, 23)
Dislocation multiplication by cross-slip and glissile reactions, see [21]:			
$\partial_t\bar{\rho}^\xi_{\text{M}} = \partial_t\bar{\rho}^\xi_{\text{M,gliss}} + \partial_t\bar{\rho}^\xi_{\text{M,cross}}$	see Eq. (14)		
Unzipping of Lomer junctions:			
$\partial_t\hat{\rho}^\xi_{\text{M}}$	see Eq. (20)		

Table 2. Overview of mechanisms, which can form mobile or network dislocation density.

Any increase of the density of the dislocation network (Eqs. (7) and (9)) inhibits the plastic slip and thus has an effect similar to a local yield stress. This idea is conceptually comparable to a formulation of dislocation dipoles as e.g. in [13, 14] and thus acts as a source of hardening. In addition to the strengthening due to junction formation, existing Lomer junctions (described by $\sum_\xi \rho^\xi_{\text{Lomer}}$) can act as obstacles to moving dislocations due to their intrinsic stress-field. This is considered by an additional hardening component $\propto \sqrt{\sum_\zeta \bar{a}_{\text{Lomer}}\rho^\zeta_{\text{Lomer}}}$ with a Lomer interaction coefficient a_{Lomer} contained in $\bar{a}_{\text{Lomer}} = 0.5a_{\text{Lomer}}$. Here, the factor 0.5 originates from the assumption that the Lomer density is shared between two slip systems. For the Lomer coefficient we choose $a_{\text{Lomer}} = 0.122$ for simplicity, which is the same value as the Lomer and self hardening coefficients in [6, 17], but represents a stress interaction with mobile dislocations instead of the strength due to the junction formation. For glissile and collinear reactions the additional hardening does not exist, since in case of the collinear reaction the lines annihilate and for glissile reactions the dislocation is mobile and included in the mobile dislocation density. The contribution of glissile, collinear and

Hirth reactions as well as self and coplanar interaction to hardening is considered by an interaction matrix $a^{\xi\zeta}$ according to [30]. The values of the hardening components are taken from [6] where the Lomer component is set to zero and replaced by the explicit incorporation of Lomer reactions (Eqs. (7) and (9)). In combination with the interaction of mobile dislocations with existing Lomer junctions explained above, we thus obtain

$$\tau^{\xi}_{\mathrm{fl,mat}} = Gb\sqrt{\sum_{\zeta}\left(a^{\xi\zeta}\left(\rho^{\zeta}_{\mathrm{M}}+\rho^{\zeta}_{\mathrm{S}}\right)+\bar{a}_{\mathrm{Lomer}}\rho^{\zeta}_{\mathrm{Lomer}}\right)}, \tag{11}$$

with the shear modulus G. The stress term $\tau^{\xi}_{\mathrm{fl,mat}}$ is incorporated into the velocity law, using the effective resolved shear stress τ^{ξ}, as

$$v^{\xi} = \begin{cases} \frac{b}{B}\left(|\tau^{\xi}| - \tau^{\xi}_{\mathrm{fl,mat}}\right)\,\mathrm{sign}\left(\tau^{\xi}\right) & \text{if } |\tau^{\xi}| > \tau^{\xi}_{\mathrm{fl,mat}} \\ 0 & \text{if } |\tau^{\xi}| \;\leq\; \tau^{\xi}_{\mathrm{fl,mat}} \end{cases} \tag{12}$$

with a friction coefficient of $B = 1\times10^{-4}$Pa s.

3.2. Dislocation reactions in the continuum

3.2.1. Formation of dislocation reactions In the course of the voxel-based investigation of the DDD data in section 2, a function between dislocation density and reaction density was motivated, which couples the dislocation activity on respective slip systems, see Eq. (1). Here, a formulation of dislocation reactions for a continuum theory in conjunction with the investigation in section 2 is derived. Since Eq. (1) formulates a relation for the reaction density present at a given dislocation state, the equation can not be directly transferred into a continuum framework which relies on a *formation rate* of dislocation reactions. However, we follow the argumentation in section 2 regarding the validity of the investigated function for all reactions shown schematically in Fig. 5 to formulate reaction equations which incorporate a slip rate according to [31, 21]. Dislocation multiplication by cross-slip and glissile reaction is incorporated into the model according to [21] and is therefore not explicitly derived here.

For the derivation of the dislocation reaction model in the context of the dislocation-based plasticity framework explained in section 3.1, we now consider the pairing of two reacting slip systems $\xi^{r'}$ and $\xi^{r''}$ individually. As a limiting criteria, at least one of the involved dislocation lines has to be mobile, i.e. $\rho^{r'}_{\mathrm{M}}, \rho^{r''}_{\mathrm{M}} > 0$ and $v^{r'} > 0$ or $v^{r''} > 0$. The stabilized dislocation density ρ^{ξ}_{S} is also a possible partner for dislocation reactions, although it does not contribute to plastic slip. Lomer junctions however are considered as obstacles for the motion of mobile dislocations, which is described by Eqs. (11) and (12). Further, we assume for simplification that the statistical variation in dislocation travel distances results in a distribution of the dislocation *link lengths* around the mean dislocation spacing, such that the *density* of all link lengths, i.e. line length times number of dislocations per volume, is constant. Using those assumptions, the mean distance of the involved dislocations on the intersecting slip systems ζ is $L^{\zeta} = 1/\sqrt{\rho^{\zeta}_{\mathrm{M}}+\rho^{\zeta}_{\mathrm{S}}}$. The

increase in reaction density is then described by a term comparable to [31, 21]:

$$\partial_t \rho_{\text{react}} = C_{\text{react}} \left(\rho_{\text{M}}^{\xi} |v^{\xi}| \sqrt{\rho_{\text{M}}^{\zeta} + \rho_{\text{S}}^{\zeta}} + \rho_{\text{M}}^{\zeta} |v^{\zeta}| \sqrt{\rho_{\text{M}}^{\xi} + \rho_{\text{S}}^{\xi}} \right) \quad \text{with } \xi, \zeta = r', r'' \text{ and } \xi \neq \zeta \tag{13}$$

with $()_{\text{react}} = ()_{\text{gliss}}, ()_{\text{Lomer}}, ()_{\text{coll}}$. Here, C_{react} is a combined coefficient similar to β in Eq. (2) which describes the effective length of the dislocation junction and contains the Burgers vector. The value range of this coefficient has been determined by DDD - simulations for glissile reactions, i.e. $C_{\text{react}} = C_{\text{gliss}}$ [32, 31]. Since Eq. (13) is valid for all reactions, the density ρ_{react} is not tied to a specific slip system and therefore does not include a slip system index.

The reaction equation (Eq. 13) describes the amount of density which is affected by the intersection of two dislocation lines forming a reaction, but it does not state if the reaction is stable. We therefore describe the stability of any junction, i.e. the irreversibility of the reaction formation, by introducing a fraction of stable dislocation reactions $\eta_{\text{react}}^{\xi}$ for all reaction types, i.e. $()_{\text{react}} = ()_{\text{gliss}}, ()_{\text{Lomer}}, ()_{\text{coll}}$. The process of a reaction formation is assumed to be irreversible for glissile and collinear reactions. Thus, it holds $\eta_{\text{gliss}}^{\xi} = \eta_{\text{coll}}^{\xi} = 1$. Whereas the collinear reaction leads to a dislocation annihilation, which is effectively a zero Burgers vector junction, the glissile reaction leads to the generation of a new mobile dislocation on a third involved slip system denoted by ξ^{gl}. It thus holds $\partial_t \rho_{\text{gliss}}^{gl} = \eta_{\text{gliss}}^{gl} \partial_t \rho_{\text{gliss}}$. Following [21], the glissile reaction leads to an increase in mobile dislocation density by

$$\partial_t \bar{\rho}_{\text{M,gliss}}^{gl} = \begin{cases} \frac{\pi}{2} \partial_t \rho_{\text{gliss}}^{gl} & \text{if } |v^{gl}| > 0 \\ \partial_t \rho_{\text{gliss}}^{gl} & \text{if } |v^{gl}| = 0 \end{cases} \tag{14}$$

and in curvature density by

$$\partial_t \bar{q}_{\text{gliss}}^{gl} = \text{sign}(v^{gl}) \pi \partial_t \rho_{\text{M,gliss}}^{gl} \sqrt{\rho} \quad \text{using} \quad \partial_t \bar{q}_{\text{gliss}}^{gl} = \frac{\partial_t \bar{\rho}_{\text{gliss}}^{gl}}{L_{\text{bow}}} \quad \text{with} \quad L_{\text{bow}} = \frac{0.5}{\sqrt{\sum_{\xi} \rho^{\xi}}} = \frac{0.5}{\sqrt{\rho}}. \tag{15}$$

Here, we assume that the glissile reaction is followed by a bow-out of the junction up to half of the mean dislocation spacing, denoted by L_{bow}, leading to the prefactor $\pi/2$ in Eq. (14).

In contrast to the glissile and the collinear reaction, the Lomer reaction creates a sessile dislocation junction which can unzip if the effective resolved shear stress τ^{ξ} exceeds a critical shear stress $\tau_{\text{cr,Lomer}}$. The latter depends on the length of the attached dislocation segments [33, 34]. We therefore assume the fraction of stable Lomer reactions $\eta_{\text{Lomer}}^{\xi}$ to scale within the interval $[0, 1]$. The increase of the density of Lomer junctions is then described by

$$\partial_t \rho_{\text{Lomer}}^{\xi} = \eta_{\text{Lomer}}^{\xi} \partial_t \rho_{\text{Lomer}} \quad \text{with} \quad \xi = r', r'' \tag{16}$$

using ρ_{Lomer} from Eq. (13) with the index $()_{\text{Lomer}}$. Although the Lomer junction crystallographically does not belong to either of the reacting slip systems, we assign the density of Lomer junctions to both involved slip systems and weight its contribution to the network dislocation density by a factor of 0.5, see Eq. (9).

3.2.2. Stability of Lomer reactions The fraction of stable Lomer reactions $\eta^{\xi}_{\text{Lomer}}$ takes into account that Lomer junctions can dissolve if a large enough shear stress, i.e. a critical stress $\tau_{\text{cr,Lomer}}$, is applied. The strength of the junction depends on the *link length*, i.e. the length of the attached dislocation lines [34, 33], which is assumed to scale with the dislocation density by $1/\sqrt{\rho}$. It thus holds $\eta^{\xi}_{\text{Lomer}} = f\left(\tau^{\xi}, \rho^{\xi}\right)$. Therefore, an intersection between two dislocation lines on two slip systems does not result in a stable Lomer junction if $\tau^{\xi} > \tau_{\text{cr,Lomer}}$. In the continuum model, $\eta^{\xi}_{\text{Lomer}}$ then acts as a prefactor in the reaction equation Eq. (16). The critical stress $\tau_{\text{cr,Lomer}}$ can be approximated to

$$\tau_{\text{cr,Lomer}} \approx 0.5Gb\frac{1}{L_{\text{Lomer}}} \tag{17}$$

based on line-tension arguments [34, 35], or based on atomistic and DDD-simulations [33, 36, 17, 37]. Here, L_{Lomer} denotes the link length, for which we assume $L_{\text{Lomer}} \propto 1/\sqrt{\rho_{\text{tot}}} = 1/\sqrt{\sum_{\xi}\rho^{\xi}}$. As introduced in section 3.2.1, we assume a distribution of link lengths due to scattering travel distances of dislocations. On both reacting slip systems $\xi^{r'}$ and $\xi^{r''}$, we thus find a maximum ($L_{\max}$) and minimum length ($L_{\min}$) of dislocation lines, which results in a distribution of the dislocation link lengths in the averaging volume between $L_{\min} < L = 1/\sqrt{\sum_{\xi}\rho^{\xi}} < L_{\max}$. Fig. 6(a) schematically shows a dislocation configuration for $L_{\min}$ and $L_{\max}$. In the following, we choose $L_{\min} = 0.1L$ and $L_{\max} = 2L$, based on the measured scattering of the travel distances and the nucleation radii of the dislocations within the DDD dislocation network [4].

Due to the relation between critical shear stress and dislocation link length (Eq. 17), there exists a longest dislocation line segment which can be stable for a given resolved shear stress

$$L^{\xi}_{\text{cr,Lomer}} = 0.5Gb\frac{1}{|\tau^{\xi}|} \quad \text{with} \quad \xi = r', r''. \tag{18}$$

This defines the weakest Lomer reaction. Fig. 6(b) schematically shows the length distribution of the dislocation segments for the general case of a different resolved shear stress on both reacting slip systems. The stress range in which stable Lomer junctions can exist is limited by $L_{\min}$ (which defines the strongest junction) and $L^{\xi}_{\text{cr,Lomer}}$ with $L^{\xi}_{\text{cr,Lomer}} = \min\left\{L^{r'}_{\text{cr,Lomer}}, L^{r''}_{\text{cr,Lomer}}\right\}$, as visualized by the green area. This means the stability of a Lomer junction is limited by the slip system with the highest shear stress. The fraction of stable Lomer reactions is then defined by

$$\eta^{\xi}_{\text{Lomer}} = \begin{cases} 1 & \text{if} \quad L^{\xi}_{\text{cr,Lomer}} \geq L_{\max} \\ \frac{L^{\xi}_{\text{cr,Lomer}} - L_{\min}}{L_{\max} - L_{\min}} & \text{if} \quad L_{\min} < L^{\xi}_{\text{cr,Lomer}} < L_{\max} \\ 0 & \text{if} \quad L^{\xi}_{\text{cr,Lomer}} \leq L_{\min}. \end{cases} \tag{19}$$

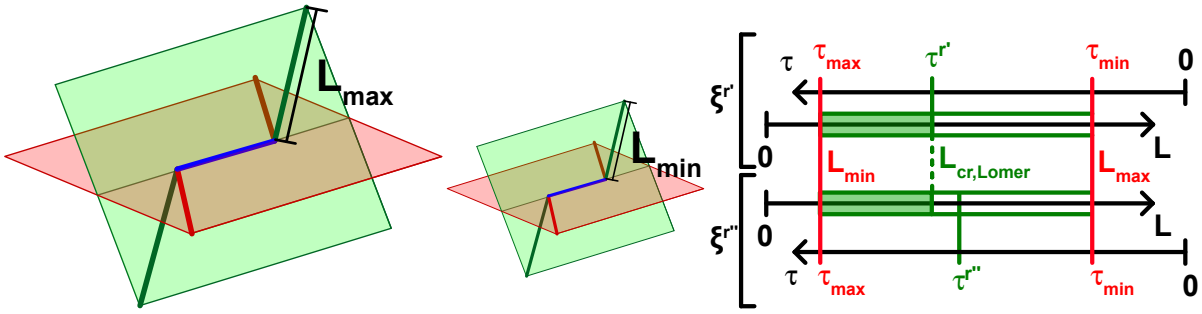

(a) Length of dislocation segments.

(b) Length distribution of dislocation segments.

Figure 6. Schematic visualization of Lomer reactions with a maximal and minimal length of the dislocation segments attached to the end-nodes of the respective reaction ($L_{\min}$ and $L_{\max}$) (a) and the stable range of segment lengths on slip systems $\xi^{r'}$ and $\xi^{r''}$, within which stable Lomer reactions can exist, visualized by the green area (b). τ denotes the applied shear on either slip system. The overall range is limited by the maximum ($L_{\max}$) and minimum ($L_{\min}$) length in conjunction with the minimum ($\tau_{\min}$) and maximum ($\tau_{\max}$) shear stress (see Eq. 18). The maximum stable segment length is limited by $L^{\xi}_{\mathrm{cr,Lomer}} = \min\left\{L^{r'}_{\mathrm{cr,Lomer}}, L^{r''}_{\mathrm{cr,Lomer}}\right\}$ on the coupled slip systems.

An increase in shear stress on at least one slip system therefore results in $\partial_t L^{\xi}_{\mathrm{cr,Lomer}} < 0$. This reproduces the physical observation of unzipping Lomer junctions, which we simplify by assuming the reverse process of the Lomer reaction formation described by Eq. (16). This means a transformation of the fraction $\left|\partial_t L^{\xi}_{\mathrm{cr,Lomer}} / \left(L^{\xi}_{\mathrm{cr,Lomer}} - L_{\min}\right)\right|$ of the density of Lomer reactions, denoted by $\hat{\rho}^{\xi}_{\mathrm{Lomer}}$, and the stabilized dislocation density $\hat{\rho}^{\xi}_{\mathrm{S}}$ into mobile dislocation density $\hat{\rho}^{\xi}_{\mathrm{M}}$. Thus it holds

$$\begin{aligned}
\partial_t \hat{\rho}^{\xi}_{\mathrm{Lomer}} &= \frac{\partial_t L^{\xi}_{\mathrm{cr,Lomer}}}{L^{\xi}_{\mathrm{cr,Lomer}} - L_{\min}} \rho^{\xi}_{\mathrm{Lomer}}, \qquad \partial_t \hat{\rho}^{\xi}_{\mathrm{S}} = \frac{\partial_t L^{\xi}_{\mathrm{cr,Lomer}}}{L^{\xi}_{\mathrm{cr,Lomer}} - L_{\min}} \rho^{\xi}_{\mathrm{S}} \\
&\text{and} \\
\partial_t \hat{\rho}^{\xi}_{\mathrm{M}} &= -\frac{\partial_t L^{\xi}_{\mathrm{cr,Lomer}}}{L^{\xi}_{\mathrm{cr,Lomer}} - L_{\min}} \left(\rho^{\xi}_{\mathrm{Lomer}} + \rho^{\xi}_{\mathrm{S}}\right) \\
&\qquad\qquad \text{with} \quad \xi = r', r'' \quad \text{if} \quad \partial_t L^{\xi}_{\mathrm{cr,Lomer}} < 0,
\end{aligned} \tag{20}$$

where $\rho^{\xi}_{\mathrm{Lomer}}$ and ρ^{ξ}_{S} is the density of Lomer reactions and the stabilized dislocation density in the given time step.

3.2.3. Impact of dislocation reactions on the dislocation line length In conjunction with [4, 21], we assume that dislocation reactions as well as cross-slip lead to a *loss* of line length on the reacting slip system. This involves line length which vanishes in the junction, i.e. the line between both junction end-nodes. The subdivision of the total dislocation density into a mobile and a network part in Eq. (7) implies that the respective loss of line length has to be broken down according to which dislocations are

able to react. This can be explained by an example: The *mobile* dislocation density on the *forest* slip system $\rho_{\mathrm{M}}^{\zeta}$ can only reduce the dislocation densities on the *primary* slip system ρ_{M}^{ξ} and ρ_{S}^{ξ} by their relative amount $\rho_{\mathrm{M}}^{\xi}/\left(\rho_{\mathrm{M}}^{\xi}+\rho_{\mathrm{S}}^{\xi}\right)$ and $\rho_{\mathrm{S}}^{\xi}/\left(\rho_{\mathrm{M}}^{\xi}+\rho_{\mathrm{S}}^{\xi}\right)$. The amount of mobile and stabilized dislocation density (denoted by the index $()_{\mathrm{M,react}}$ and $()_{\mathrm{S,react}}$) which is lost on reacting slip systems due to the formation of any dislocation reaction with a specific length is derived as

$$\begin{aligned}
\partial_t \rho_{\mathrm{M,react}}^{\xi} &= -\eta_{\mathrm{react}}^{\xi}\, C_{\mathrm{react}} \left(\rho_{\mathrm{M}}^{\xi} |v^{\xi}| \sqrt{\rho_{\mathrm{M}}^{\zeta} + \rho_{\mathrm{S}}^{\zeta}} + \rho_{\mathrm{M}}^{\zeta} |v^{\zeta}| \sqrt{\rho_{\mathrm{M}}^{\xi} + \rho_{\mathrm{S}}^{\xi}} \frac{\rho_{\mathrm{M}}^{\xi}}{\rho_{\mathrm{M}}^{\xi} + \rho_{\mathrm{S}}^{\xi}} \right) \\
&\text{and} \\
\partial_t \rho_{\mathrm{S,react}}^{\xi} &= -\eta_{\mathrm{react}}^{\xi}\, C_{\mathrm{react}} \left(\rho_{\mathrm{M}}^{\zeta} |v^{\zeta}| \sqrt{\rho_{\mathrm{M}}^{\xi} + \rho_{\mathrm{S}}^{\xi}} \frac{\rho_{\mathrm{S}}^{\xi}}{\rho_{\mathrm{M}}^{\xi} + \rho_{\mathrm{S}}^{\xi}} \right) \\
&\qquad\qquad \text{with} \qquad \xi, \zeta = r', r'' \quad \text{and} \quad \xi \neq \zeta.
\end{aligned} \tag{21}$$

This equation holds for all considered dislocation reactions, i.e. $()_{\mathrm{react}} = ()_{\mathrm{gliss}}, ()_{\mathrm{Lomer}}, ()_{\mathrm{coll}}$. The sum of both contributions in Eq. (21) thus equals the negative production rate of the density of dislocation reactions ρ_{react} in Eq. (13) multiplied with the fraction of stable dislocation reactions $\eta_{\mathrm{react}}^{\xi}$:

$$\eta_{\mathrm{react}}^{\xi} \partial_t \rho_{\mathrm{react}} = -\left(\partial_t \rho_{\mathrm{M,react}}^{\xi} + \partial_t \rho_{\mathrm{S,react}}^{\xi} \right) \quad \text{with} \quad \xi = r', r''. \tag{22}$$

Here, $\eta_{\mathrm{react}}^{\xi}$ equals 1 for glissile and collinear reactions and is determined by Eq. (19) for Lomer reactions.

The stabilized dislocation density ρ_{S}^{ξ} describes the line length of dislocations which are attached to the end-nodes of Lomer junctions, as shown in Fig. 6(a). The increase of ρ_{S}^{ξ} thus results from a stabilization of mobile dislocations involved in Lomer dislocation reactions. This contribution is denoted by $\partial_t \bar{\rho}_{\mathrm{M,Lomer}}^{\xi}$ and is assumed to be reversely proportional to the reduction of mobile dislocation density due to Lomer junction formation (Eq. (21) with index $()_{\mathrm{Lomer}}$), leading to

$$\partial_t \rho_S^{\xi} = \partial_t \bar{\rho}_{\mathrm{M,Lomer}}^{\xi} = -\partial_t \rho_{\mathrm{M,Lomer}}^{\xi} \quad \text{with} \quad \xi = r', r''. \tag{23}$$

In conjunction with the subdivision of the total dislocation density (Eq. 7), we also assume that a related part of the curvature density does not contribute to the expansion of existing dislocations. This reproduces the observation made in DDD simulations that dislocation networks mainly consist of straight lines, where the dislocation curvature is concentrated in end-nodes of dislocation junctions [4]. Following the argumentation in [21], we reproduce this behavior by reducing the curvature density q^{ξ} based on the argument of a reduction of 'potential' of line length increase by dislocation expansion due to the dislocation reaction. Therefore, the reduction of line length (Eq. 21) necessarily leads to a proportional reduction in curvature density. We obtain the final formulation for the reduction of curvature density on the reacting slip systems $\xi^{r'}$ and $\xi^{r''}$ by a modification of the underlying equation in [21]:

$$\partial_t q_{\mathrm{react}}^{\xi} = \eta_{\mathrm{react}}^{\xi} C_{\mathrm{q}} \frac{\partial_t \rho_{\mathrm{react}}}{\rho_{\mathrm{react}}^{\xi}} q_{\mathrm{M}}^{\xi} \quad \text{with} \quad \xi = r', r'' \quad \text{and} \quad ()_{\mathrm{react}} = ()_{\mathrm{gliss}}, ()_{\mathrm{Lomer}}, ()_{\mathrm{coll}}, \tag{24}$$

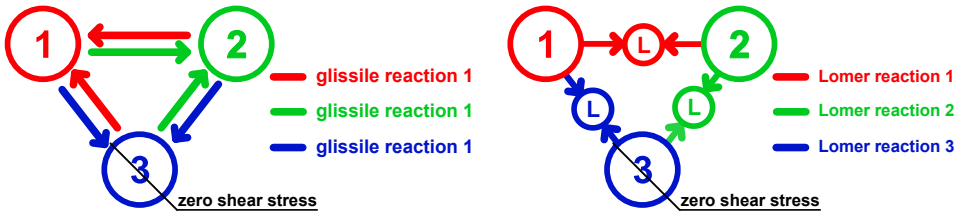

Figure 7. Schematic overview of three considered slip systems $\xi = 1, 2, 3$ with respective glissile and Lomer reactions.

where we choose $C_{\mathrm{q}} = 2$ according to [21] unless defined otherwise.

3.3. Considered systems

3.3.1. Simplified system First, we only consider glissile and Lomer reactions by using a configuration of three slip systems, as shown schematically in Fig. 7. We exclude all spacial gradients in the evolution equation Eq. (10), which results in a system of ordinary differential equations. The spacial orientation of the slip systems is not related to any real crystallographic orientation. Thereby, the system is artificial, but comes with the benefit to reduce the complexity in order to focus on the interplay of dislocation multiplication and dislocation network formation. The system is therefore fully homogeneous and serves as a benchmark configuration. Two slip systems $\xi = 1$ and $\xi = 2$ are subjected to a constant shear stress of $\tau_{1,\mathrm{ext}} = \tau_{2,\mathrm{ext}} = 15$ MPa. On the third slip system $\xi = 3$, we set $\tau_{3,\mathrm{ext}} = 0$, in order to mimic active and inactive slip systems. The initial dislocation density is chosen as $\rho^{\xi} = \rho^{\xi}_{\mathrm{M}} = 1 \times 10^{12}\mathrm{m}^{-2}$ with $q^{\xi} = 0$ initially on each slip system. Due to the neglected transport terms it further holds $\|\boldsymbol{\kappa}^{\xi}\| = 0$. In order to determine the influence of Lomer junctions as obstacles for the movement of mobile dislocations, we investigate the impact of the additional interaction stress given by Eq. (11) using $a_{\mathrm{Lomer}} = 0.122$. For the simple system, the interaction matrix $a^{\xi\zeta}$ is chosen to equal zero to solely focus on the influence of the Lomer reaction as obstacles. The reaction coefficient $C_{\mathrm{react}} = 0.064$ in Eq. (13) is chosen according to [21] for glissile and Lomer reactions. The elastic material parameters are given by the elastic modulus $E = 71.3$ GPa, a Poisson's ratio of $\nu = 0.34$ and a Burgers vector of $b = 0.256$ nm.

3.3.2. Full fcc system with tensile loading In a second step, we use all 12 fcc systems and investigate the full model consisting of glissile, Lomer, collinear reactions and cross-slip. We aim to compare the average dislocation density evolution as well as the spacial density distribution to the DDD-simulations of [4]. We therefore apply the model to a cubic volume with edge length of $(5\times5\times5)\,\mu$m, as in [4, 21]. The system is subjected to a tensile displacement on two opposite normal surfaces in the direction of the [100] crystal axis using a constant strain rate of $\dot{\varepsilon} = 5000\,\mathrm{s}^{-1}$. This leads to a high symmetry multislip orientation in which eight slip systems have the same nonzero Schmid-factor (further called *active*) and four slip systems have a zero Schmid-factor (further called *inactive*).

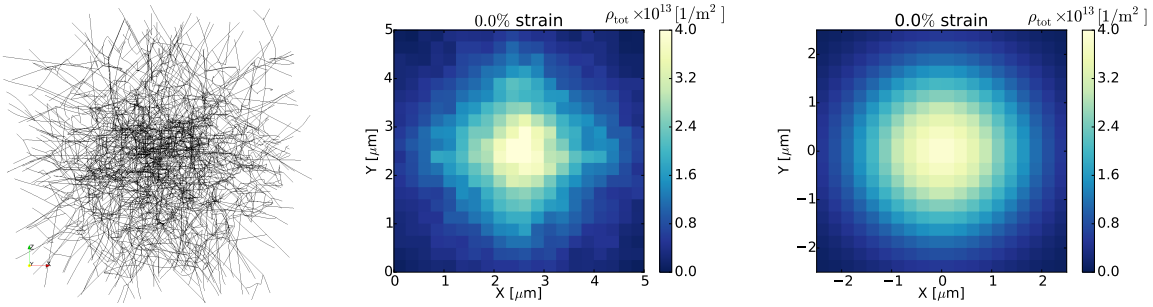

(a) Relaxed initial dislocation microstructure of one representative DDD simulation.

(b) Ensemble-average of seven initial dislocation microstructures of DDD.

(c) Initial dislocation density distribution in CDD.

Figure 8. Relaxed initial dislocation microstructure of one representative DDD simulation (a); Ensemble-average of seven DDD simulations, averaged over $20 \times 20 \times 1$ voxels (b); Initial distribution of the total dislocation density $\rho_{\text{tot}} = \sum_\xi \rho^\xi$ in the CDD simulation averaged over the tensile direction (c). The voxel-plot in (c) serves as a comparison to the averaged DDD distribution, but does not show the actual mesh used in the simulation, which is tetragonal.

We set $v = 0$ on the inactive slip systems to avoid dislocation activity triggered by boundary conditions.

The initial dislocation density distribution is chosen to reproduce the spacial features of the initial dislocation microstructure of the DDD simulations [4]. The latter originates from a relaxation of a random distribution of dislocation loops, shown in Fig. 8(a). The ensemble-average of seven relaxed DDD microstructures is shown in Fig 8(b). Here, the dislocation line length is averaged over $20 \times 20 \times 1$ voxel, averaging over the full system in tensile direction (here normal to the drawing plane). It can be seen that the dislocation density accumulates in the center of the system. For the continuum simulation, we mimic this initial microstructure by distributing the total dislocation density ρ^ξ on each slip system ξ according to a multivariate normal distribution using a vector of the mean value equal to $0\,\mu$m and standard deviations of $\sigma_x = \sigma_y = \sigma_z = 1.2 \times 10^{12}\,\text{m}^{-2}$ in the respective coordinate directions x, y and z. This results in an accumulation of dislocation density in the center of the system, as shown in Fig. 8(c). This initial dislocation configuration consists of *network dislocation density* ρ^ξ_{net}, which reproduces the stable dislocation network observed in [4]. For the average initial dislocation density per slip system ξ it holds $\rho^\xi_{\text{Lomer}} \approx 0.35 \times 10^{12}\,\text{m}^{-2}$ and $\rho^\xi_{\text{S}} \approx 0.75 \times 10^{12}\,\text{m}^{-2}$, i.e. one third of the line length per slip system is stored in Lomer junctions, which resembles the configuration in [4]. This results in a total dislocation density of $\rho_{\text{tot}} = \sum_\xi \rho^\xi \approx 1.13 \times 10^{13}\,\text{m}^{-2}$, when averaged over all slip systems. Further, we choose $\rho^\xi_{\text{M}} = 0$, $\|\boldsymbol{\kappa}\|^\xi = 0$ and $q^\xi = 0$ initially. For the analysis, we use the interaction stress according to Eq. (11) with a non-zero interaction matrix in order to reproduce the mutual obstruction of coupled dislocation segments.

Following the comparison with the DDD simulations, we investigate the interplay

between dislocation fluxes and dislocation network evolution by first excluding all spacial gradients (local simulation) and afterwards allowing for dislocation fluxes (nonlocal simulation). The reaction coefficients in Eq. (13) are chosen as $C_{\mathrm{gliss}} = C_{\mathrm{Lomer}} = C_{\mathrm{coll}} = 0.032$ for the local simulation, i.e. all reactions are weighted equally. For the nonlocal simulation, we choose $C_{\mathrm{gliss}} = C_{\mathrm{Lomer}} = 0.064$, $C_{\mathrm{coll}} = 0.032$ and $C_{\mathrm{q}} = 1$ in Eq. (24), which means that we increase the effect of the dislocation multiplication in order to compensate for the dislocation flux. The dislocation flux necessarily leads to a loss of dislocation density through the outer system boundaries and thus a decreasing density by using the same parameters as for the local simulation. The elastic constants are chosen as before.

4. Results

In order to analyze the behavior of the model derived in section 3 regarding the interplay between dislocation multiplication and stabilizing mechanisms, we first consider the simplified system explained in section 3.3.1. Afterwards, we apply the full model to the fcc system setup explained in section 3.3.2 and compare the results to DDD simulations and investigate the influence of the flux terms in the evolution equation of the dislocation system on the spacial dislocation density distribution.

4.1. Simplified system of glissile and Lomer reactions

In a first analysis, we reduce the model to only account for glissile and Lomer reactions in a configuration which consists of three slip systems, as shown in Fig. 7. The system is fully homogeneous since spacial derivatives in the evolution equations of the dislocation densities (Eq. (10)) are excluded. In a first analysis, we assume a constant dislocation velocity which originates from an external shear stress of $\tau^{\xi}_{\mathrm{ext}} = 15\,\mathrm{MPa}$ on the slip systems $\xi = 1$ and $\xi = 2$, i.e. it holds $v^{\xi} = \frac{b}{B}\tau^{\xi}_{\mathrm{ext}}$. Slip system 3 is inactive, making these dislocations passive reaction partners.

The evolution of the dislocation densities representing the line lengths within dislocation networks (total dislocation density $\rho^{\xi}_{\mathrm{tot}}$, mobile dislocation density ρ^{ξ}_{M} and network dislocation density $\rho^{\xi}_{\mathrm{net}}$) is shown in Fig. 9(a) per slip system over the simulation time. The total dislocation density on both active slip systems increases tenfold before showing a saturation. On the inactive slip system the dislocation density increases due to glissile reactions and reaches about half the density on active slip systems at the end of the simulation. At this point, the total dislocation density almost completely consists of network dislocation density $\rho^{\xi}_{\mathrm{net}}$, i.e. all dislocations contribute to configurations stabilized by Lomer junctions. A close-up on the initial part of the simulation in Fig. 9(b) shows an initial increase in mobile dislocation density on both active and inactive slip systems. After a simulation time of about $0.4\,\mu\mathrm{s}$, the mobile density decreases along with an increase of the network dislocation density $\rho^{\xi}_{\mathrm{net}}$.

Since in this simplified configuration the system behavior is largely determined by

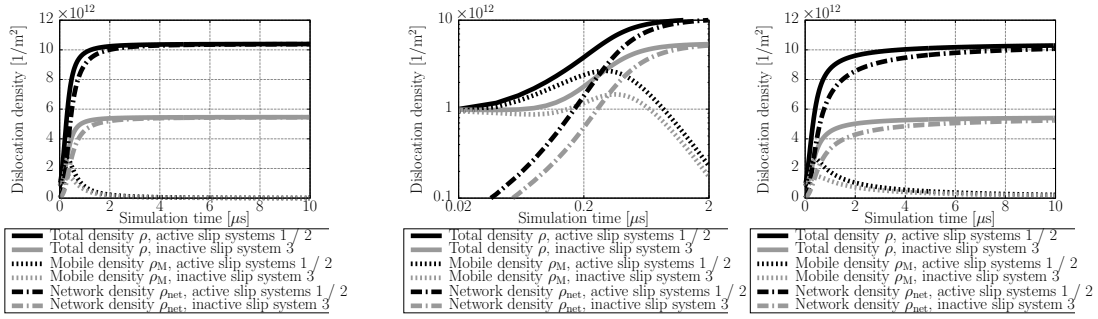

(a) Full simulation time, without flow-stress.

(b) Initial phase from (a).

(c) Full simulation time, with flow-stress.

Figure 9. Evolution of dislocation densities describing the dislocation network (Eqs. (7) and (9)) per slip system without an additional flow-stress term showing the full simulation time (a) and the initial phase of the simulation (b). (c): same as (a), but with an additional flow-stress term, see Eq. (11).

the Lomer reaction, it is feasible to account for an obstacle-effect of Lomer junctions on remaining mobile dislocations. As explained in section 3.1.2, this is incorporated into the model by a short-range interaction stress according to Eq. (11) using a coefficient of $a_{\mathrm{Lomer}} = 0.122$. By choosing $a^{\xi\zeta} = 0$ in Eq. (11), we solely focus on the influence of Lomer junctions for simplicity. In this case, the dislocation velocity is then a function of the dislocation density, as described by Eq. (12). The respective evolution of the dislocation densities over simulation time is shown in Fig. 9(c). The system shows a relaxation into a stable network configuration, which does not qualitatively differ from the system behavior without an additional interaction stress (Fig. 9(a)). However, the mobile dislocation density decreases only gradually until the end of the simulation.

The evolution of the curvature density on active slip systems displayed in Fig. 10(a) shows an initial increase due to glissile reactions followed by a decrease nearly until disappearance. Similar to the evolution of the mobile dislocation density in Fig. 9(c),

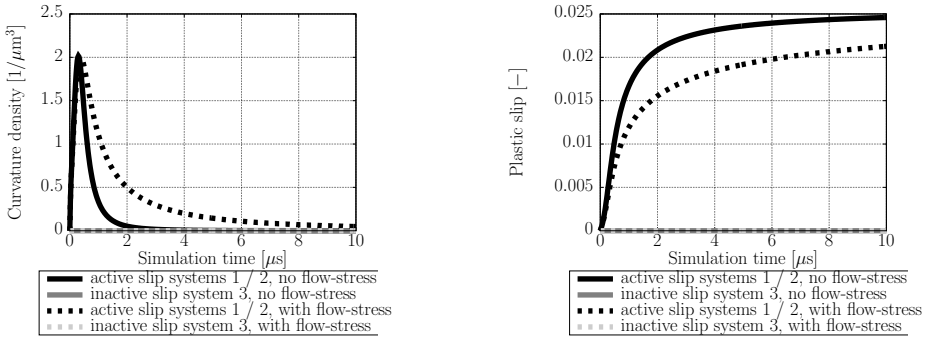

(a) Curvature density.

(b) Plastic slip.

Figure 10. Evolution of the curvature density (a) and the plastic slip (b) per slip systems, comparing the simulations with and without the additional flow-stress term Eq. (11).

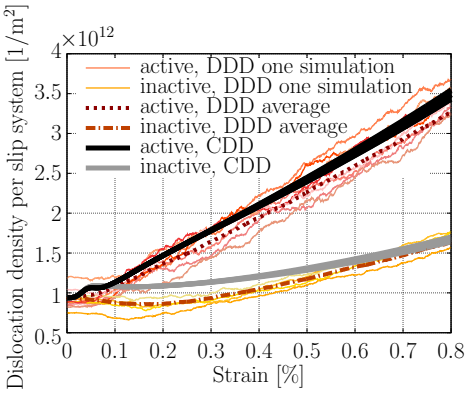

(a) Dislocation density per slip system.

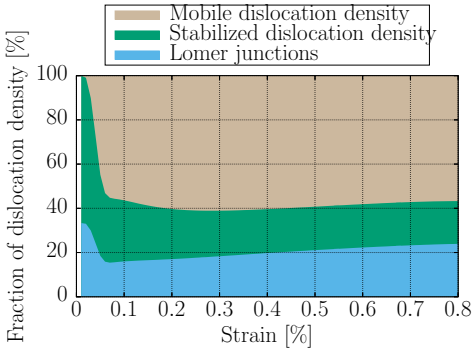

(b) Fraction of dislocation densities (CDD).

Figure 11. (a): Evolution of the dislocation density per slip system using all explicitly modeled dislocation mechanisms, as shown in Fig. 5, compared to one DDD simulation and an average over 10 DDD simulations from [4]. (b): Total density subdivided into contributions from the mobile dislocation density and the network dislocation density as a fraction of the total dislocation density as a function of total strain, summarized over all slip systems. Local simulation containing no dislocation fluxes.

the decrease of the curvature density is delayed by using the additional interaction stress. Fig. 10(b) shows the evolution of the accumulated plastic slip for the simulations with and without the interaction stress Eq. (11). Here, a saturation of the plastic slip on active slip systems is observed after an initial increase. By using the additional interaction stress, a lower accumulated plastic slip is observed almost for the entire simulation time. However, the initial increase of the plastic slip on active slip systems is almost the same for both cases, since the initial configuration consists of mobile dislocations only.

4.2. Full fcc system with tensile loading

In a second analysis, we evaluate the performance of the continuum model including all dislocation mechanisms as visualized in Fig. 5 by comparing the evolution of the dislocation microstructure with DDD results published in [4]. Therefore, we apply the continuum model to the system configuration explained in section 3.3.2. For a first investigation, we exclude spacial derivatives in the evolution equation of the dislocation densities.

The evolution of the averaged total dislocation density per slip system compared to the DDD results is shown in Fig. 11(a) for active and inactive slip systems. The dislocation density on active slip systems increases nearly linearly after obtaining a stable plastic flow in both CDD and DDD. On inactive slip systems, the increase in dislocation density is much less pronounced as on active slip systems which matches the DDD results. Overall, a close accordance between CDD and DDD can be observed after about 0.1% strain.

The initial phase of the simulation is characterized by a mobilization of the

dislocation network in both CDD and DDD. However, in the CDD simulation this leads to a short increase in density due to the dissolution of Lomer junctions, which is not observed in DDD the same way. In order to closer investigate the interplay of dislocation multiplication and the stabilizing processes in the continuum model, the breakdown of the total dislocation density into its contributions (ρ_{M}, ρ_{net} and ρ_{S}) summarized over all slip systems is shown Fig. 11(b). The figure shows the evolution of the respective densities as fraction of the total dislocation density over strain. Here, it is clearly observed that initially no mobile dislocation density is present. Upon loading, the fraction of network dislocation density decreases rapidly to about 40% which increases mobile density. During this process, the fraction of Lomer junctions decreases from about 30% to just below 20% which explains the initial rise in density observed in Fig. 11(a). However, after this initial mobilization phase, the distribution between mobile and network density remains relatively stable with a division of around 60% to 40%. Corresponding results by considering dislocation fluxes in the evolution equations, i.e. the nonlocal simulation, using model parameters as outlined in section 3.3.2 show a comparable behavior, as shown in Appendix A.

Finally, we compare the evolving dislocation microstructure in the continuum simulation to the DDD prediction. Fig. 12 displays snapshots taken from various stages of the DDD and CDD simulations, showing the spacial dislocation distributions. For a reasonable comparison between CDD and DDD, we transform the discrete dislocation lines of seven DDD simulations (shown in Fig. 12(a) for one simulation) into a two-dimensional representation of a dislocation density field as explained in section 3.3.2. The dislocation density distribution obtained by this averaging is shown in Fig. 12(b). It can be observed that dislocations which initially are already concentrated in the center of the system continue to accumulate during loading until 0.8% tensile strain. In contrast, the areas close to the boundaries remain relatively dislocation free. This applies especially to the corners and edges of the simulation volume. A similar accumulation of dislocation density is also observed in the corresponding representations of the CDD simulations, shown in Fig. 12(c) for the local simulation and in Fig. 12(d) for the nonlocal simulation. However, certain differences occur between the local and the nonlocal simulation in the later stages of the simulation. The dislocation density in the local simulation also increases in areas close to the boundaries, which is not observed in this form in either the DDD or the nonlocal CDD formulation.

5. Discussion

We introduce a dislocation-density-based continuum model for the evolution of dislocation networks, which combines dislocation multiplication with a formation of stable dislocation network structures. In order to find links between DDD and the continuum scale, we use methods of data science to characterize the discrete dislocation microstructure. This preliminary investigation serves as motivation for the continuum model of dislocation network evolution, where the latter is investigated in a simplified

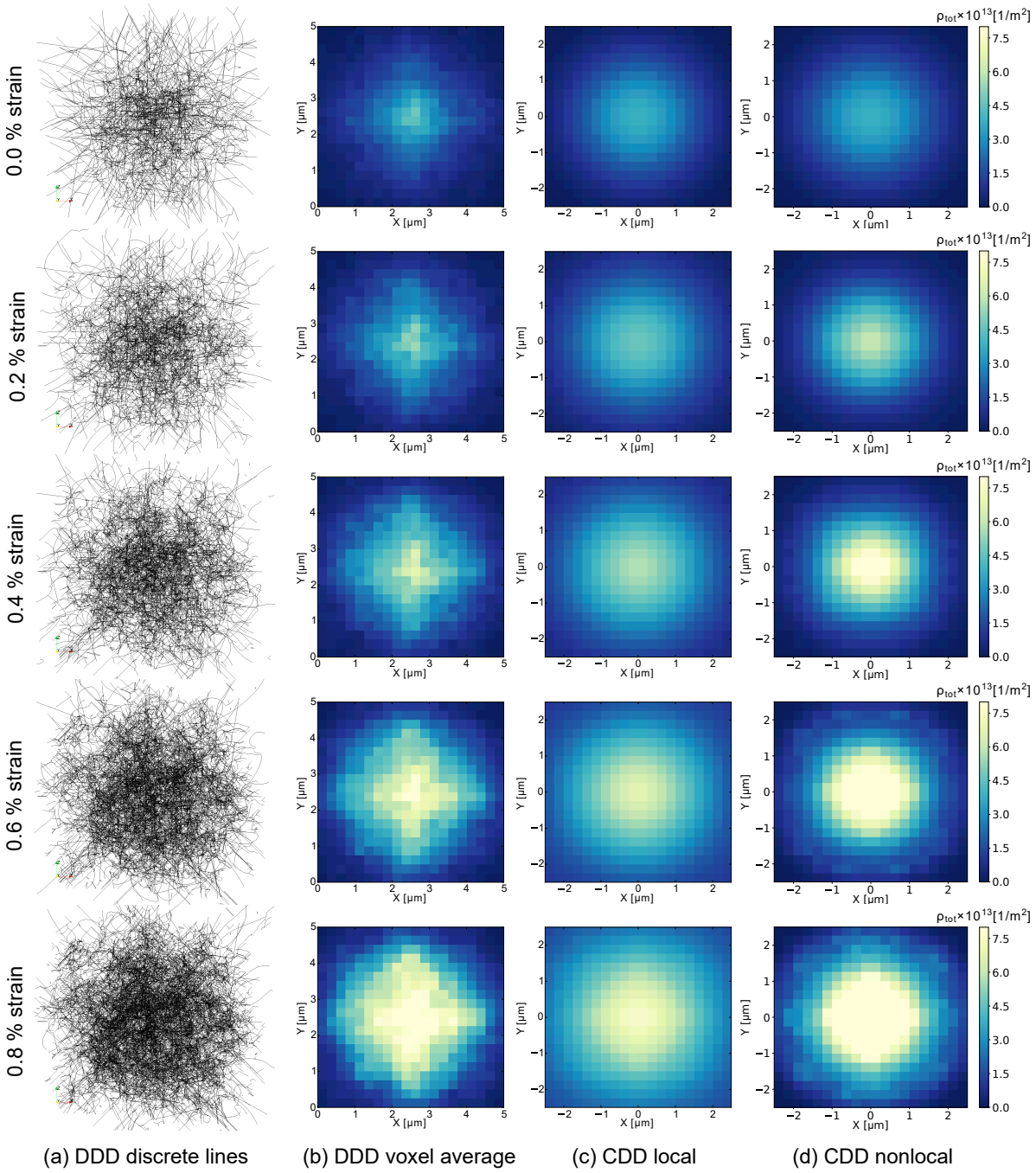

Figure 12. Overview of dislocation microstructures obtained from DDD simulations [4] and from the continuum model for 0.0%, 0.2%, 0.4%, 0.6% and 0.8% total strain. Top view of one representative DDD simulation consisting of discrete lines (a); Ensemble-average of seven DDD simulations, averaged over $20 \times 20 \times 1$ voxels (b) and distribution of the total dislocation density summarized over all slip systems averaged over the tensile direction for the local (c) and the nonlocal continuum simulation (d). The voxel-plots in (c, d) serve as a comparison to the averaged DDD distribution (b), but do not show the actual mesh used in the simulation, which is tetragonal.

system to isolate the mechanisms, complemented by a tensile test of the full fcc system.

Given the complexity of the DDD network, manageable data sets for the analysis of the dislocation microstructure by methods of data science have to be provided. Here, the data set is obtained by generating continuum field variables by averaging the dislocation characteristics such as the line length over the system volume, which is subdivided into voxels. The increase in the number of dislocations in conjunction with the reaction density on trend, shown in Fig. 2, indicates that the increase in reaction density mostly originates from the formation of new dislocation reactions, instead of an elongation of the junction lines. This observation motivates the assumption of a function describing the present density of dislocation reactions which is valid for all reaction types (Eq. (1) and Eq. (2)). By applying different scaling coefficients, i.e. β, $\beta^{\xi\zeta}$ or $\beta_1^{\xi\zeta}$ resp. $\beta_2^{\xi\zeta}$, we vary the aggregation of the slip system pairings and thus compare different degrees of homogenization of the dislocation interaction for the same reaction type. This is conceptually analogous to the investigation in [38] which compares the different homogenisation originating from the popular flow-stress term according to [8, 9] in contrast to proposed interaction matrix by [30]. The results of the prediction with the multiple linear regression model on Eq. (1) demonstrate not only the existence of a relation between dislocation density and reaction density, but also confirms the validity of the assumption to use the same relationship for all reactions, as shown in Fig. 3. Further, the temporal split between test and training set implies that the model predicts the reaction density of future time steps based on a training on earlier stages of the simulation. The very minimal difference between the prediction on the training set compared to the test set, as shown in Table 1, underlines the solidity of the model and thus the validity of the approach.

By comparing different feature sets in Table 1, basically no influence of coalescing each slip system pair (Eq. (1) using $\beta_1^{\xi\zeta} = \beta_2^{\xi\zeta}$) on the prediction quality is observed. For the continuum theory, this means that combining the original and reverse order of primary and forest system into a single reaction equation as done in Eq. (13) is a valid simplified approach. Further, the complexity of the model is significantly reduced by combining all slip system pairings of the specific reaction type into a single feature set (Eq. 2). However, the drop in prediction quality indicates that a common factor independent of the pairing might oversimplify the individual contribution of each slip system. This argument is supported by the feature selection technique of reducing the number of coefficients, which leads to a varying model prediction quality when considering different slip system pairs. Further, the correlation between the *individual* dislocation densities and the overall reaction densities shows a very high scatter and a lower average correlation compared to the respective correlations of the coupling terms (Eq. (1) and Eq. (2)), see Fig. 4. These results indicate that while the combination of all slip systems might lead to a reasonable prediction on average, the individual contribution of each slip system and slip system pairing on the overall reaction density can largely differ. Physically this means that the line length of a forming dislocation junction is not the same for all slip system combinations. It is noteworthy that this scatter is already

observed in the present high symmetry configuration which is characterized by a clear separation between active and inactive slip systems with respect to the Schmid-factors. Since the investigated setup is already the most ideal scenario of multislip loading, it can be expected that the differing influence of slip systems will increase in basically any other loading condition and potentially even in the given one for higher strains.

The results from the preliminary investigation of the DDD dislocation network further supports conclusions made earlier in [4, 5, 21] that the contribution of individual slip systems to dislocation multiplication and dislocation network formation are an important feature to include in slip-system-based continuum models. What is even more significant, however, is that the in-depth analysis of the DDD data motivates functional relations for slip systems coupling to describe the contribution of all relevant dislocation reactions to network formation by continuum field variables. The interplay between slip systems is thus not limited to the aspect of dislocation multiplication by glissile reactions, as shown in [21, 31], but also for the formation of stable structures and for collinear annihilation in dislocation networks. Since the examined functions in section 2 only relate the dislocation state to the present dislocation reaction densities, i.e. the line lengths of the junctions, the results of the voxel analysis can not be directly transferred into rate equations for the continuum framework. However, the results confirm the importance of incorporating the interplay of slip systems to reflect dislocation reactions. Therefore, we use this conclusion as a motivation to formulate dislocation reaction equations in the CDD framework based on coupling terms similar to [21, 31] which are valid regardless of the specific reaction type..

The investigation of the continuum model in the simplified system combines the aspect of dislocation expansion, which follows dislocation multiplication incorporated from [21], with a formation of stable dislocation structures in a minimal benchmark configuration. Those mechanisms are reproduced in terms of internal variables by modifying the dislocation density due to dislocation expansion or dislocation reactions and the curvature density. For the simple system, the coupling of those mechanisms results in an increase of dislocation density by dislocation multiplication and a subsequent saturation due to formation of dislocation networks as shown in Fig. 9(a). The density increase implies a reduction in dislocation spacings, respectively link lengths, in the network, see Eq. (18, 19). The saturation of the dislocation density over time is in conjunction with the saturation of the plastic slip (see Fig. 10(b)) caused by an increase in the fraction of stable Lomer junctions (Eq. 19) at a given stress. Thereby, the contribution of the Lomer reaction increases upon the generation of new dislocations through glissile reactions and a subsequent increase in density, limiting the plastic slip generated by each dislocation. This mechanism has been described in [4] in the context of dislocation networks and is adequately reproduced by the continuum model. Although the evolution of the total density resembles the characteristics of the similar system investigated in [21], the observed mechanism in the current study is solely caused by formation of sessile junctions, even without any additional 'flow-stress' term. This perspective of treating Lomer and collinear reactions as comparably important

for dislocation networks as glissile reactions is also supported by the observations of a comparable density increase of all considered reactions in the preliminary data analysis, see Fig. 3.

The decrease of the curvature density along with the formation of the dislocation network (Fig. 10(a)) reproduces the observed microstructure consisting of straight lines, which implies a concentration of the system curvature into the endpoints of dislocation junctions. This concentrated curvature is relatively stable and does not lead to an expansion of dislocations in the way it is described by the kinematic formulation of the CDD theory (Eq. 5). The anti-proportional behavior of the decrease of curvature density (Fig. 10(a)) compared to the formation of the dislocation network (Fig. 9(a)) can then be interpreted as a mechanism which counteracts the increase of curvature due to generation of new dislocations and thus contributes to the stability of the dislocation network. As conclusion for the simplified system, an accordance of the proposed continuum model with observations in DDD simulations can be drawn: (I.) Expansion of individual dislocations is limited by their involvement in dislocation reactions. (II.) The emerging dislocation network is relatively stable and consists of straight dislocation lines with varying segment lengths and concentrated curvature in dislocation junctions.

The formulation of a dislocation density which is distributed into a mobile part (ρ_{M}) and a part which does not directly contribute to plastic slip (ρ_{net}) allows for the formulation of an initial condition which reproduces stable dislocation networks. In the full fcc system, mobile dislocation density is not present initially and can thus only be generated by mobilization of the initial dislocation network upon loading. This explains the characteristic of the dislocation density evolution in the initial simulation phase, shown in Fig. 11(a). The onset of plasticity is determined by the 'strength distribution' of Lomer junctions, where yielding originates from the mobilization of the weakest junctions, i.e. the junctions with the longest link length (attached dislocation lines). Since the mobilization of the Lomer junction as considered here typically increases the line length, the initial yield behavior avoids a decrease of the dislocation density below the initial value in the nonlocal simulation (shown in Fig. A.1(a) in Appendix A). For simplicity, the formation and dissolution of dislocation reactions is concentrated into a single numerical time step. However, reaction processes can take place over a longer period of time and are influenced by the surrounding microstructure. This might serve as an explanation for the short increase of the density right after overcoming the yield point in CDD (Fig. 11(a) and Fig. A.1(a)). It is also likely that a more accurate distribution of link lengths, as shown in [5], will influence the dislocation behaviour in the initial part of the simulation.

Besides, an increase of the total dislocation density per slip system is observed which is very close to the DDD prediction on active and inactive slip systems for the vast majority of the simulation time for the local simulation (Fig. 11(a)). Furthermore, the uniform fractional distribution of the average mobile and network dislocation densities shown in Fig. 11(b) indicates a stable interplay of all considered mechanisms. Thus, the dislocation multiplication is in balance with mechanisms that either annihilate (collinear

reaction) or stabilize line length (Lomer reaction) within the network. The results show that this interplay of dislocation reactions is able to reproduce observations in DDD simulations [4], where it is shown that cascades of multiplication events produces further plasticity, which in turn is limited by other reactions. This conclusion holds also for the nonlocal simulation shown in Fig. A.1(b) in Appendix A. However, the average dislocation density increase is slightly nonlinear, as shown in Fig. A.1(a). The system areas closer to boundaries contain relatively low density (see the density distribution in Fig. 12(d)), but carry a large percentage of the total volume. Therefore, even a slight overestimation of the dislocation activity in these areas can have a large impact on the total density. This overestimation is likely to originate from an inaccurate reproduction of dislocation mechanisms at very low dislocation densities in the continuum, which in DDD are characterised by statistical effects.

This difference in average density evolution motivates a deeper examination of the spacial dislocation density distribution obtained from the CDD simulations, which is shown in Fig. 12. The comparison with averaged DDD results demonstrates that the local and the nonlocal CDD simulation is able to resolve the concentration of the dislocation network in the center of the system and its continuous densification. Those are important microstructural features, which originate from the limited expansion of individual dislocations. However, the local simulation (Fig. 12(c)) predicts a noticeable density increase at the boundaries of the system, which is not observed in either the DDD or the nonlocal CDD simulation. In this respect, the distribution obtained from the nonlocal simulation (Fig. 12(d)) is closer to DDD due to the outflow of the density at the boundaries and a transport of dislocations into the center of the system. It might not be very surprising that the nonlocal simulation as opposed to the local simulation is able to capture such effects, since they ultimately arise from the mere existence of the nonlocal terms. However, it should be noted that the examined simulation volume with $(5\,\mu\mathrm{m})^3$ is relatively small for a continuum theory. It is naturally to be expected that any boundary effect will have lower impact in larger simulation volumes. In conjunction with the very promising per-slip-system results for the local simulation (Fig. 11) the results raise the question to what extend the incorporation of dislocation transport terms decisively determine the microstructural evolution. However, this question can not conclusively be answered in the present study.

Summarizing, the study presents an approach that combines the dislocation multiplication with the formation and evolution of dislocation networks in a continuum theory. This approach mimics the complexity of dislocation microstructures observed in DDD [4, 5] and resembles similar models of dislocation dipoles in single slip [13, 14]. The investigation of the averaged DDD data by data science methods shows that even in an ideal system dislocation reactions which determine the overall system behavior are influenced by individual slip systems. This opposes approaches for dislocation multiplication based on the Kocks-Mecking theory [8], as well a slip-system-wise adoption of 'flow-stress' terms in the velocity law (Eq. 12) as the only source of strain hardening. Contrary to the presented model, such terms either allow for an expansion

of *all* dislocations or stop the plastic slip completely. The main feature of the presented model is thus the separation of the mechanism that causes the plastic slip, i.e. the dislocation expansion, from the mechanisms that modify the *rate* of the plastic slip either by generating new dislocations or by limiting their expansion on average. Due to the explicit incorporation of dislocation reactions using their crystallographic slip system pairings, dislocations on all slip systems have a significant impact on the mobility of dislocations on individual slip systems. Furthermore, the effective mobility of the dislocation network is determined by range of critical stresses to unzip dislocation junctions, which weakens the average dislocation spacing as a descriptive variable as specified by the Kocks-Mecking theory [8] to some extend.

However, several open questions remain with respect to the analysis of dislocation networks as well as for modeling those in the CDD formulation. For the continuum model, it was assumed for simplification purposes that the reaction parameters are independent of the specific slip system pairing. However, according to the results of the DDD data analysis, different reaction parameters for different slip system pairings might be reasonable, indicating an analogy to the 'interaction matrix' compared to the 'Taylor' flow-stress. Further, the boundary between mobile dislocations and sessile objects is typically less clear as assumed by the Lomer junctions in the current model. In this respect, it is to be determined how the character of dislocation networks is reflected in other system configurations, since real deformation processes rarely occur as homogeneously as assumed here. An extension of the investigation into more heterogeneous deformation conditions may therefore include non-high symmetry crystal orientations, loading conditions containing stress gradients, or the formation of dislocation cell structures resulting in locally different slip system activities.

6. Conclusion

We introduce a model for the evolution of dislocation networks in a dislocation-based formulation of crystal plasticity, which provides an approach for a homogenization of the interaction between dislocation multiplication and the stabilization of the emerging dislocation network. By using data-driven methods, we analyze a DDD dislocation network to identify microstructural characteristics and derive continuum equations for relevant dislocation reactions, which are incorporated into the continuum model using their crystallographic slip system pairings.

The analysis of the DDD network by data science methods shows that despite the ideal high-symmetry crystal orientation, the overall evolution of dislocation networks and thus the system behavior can be determined by individual slip systems and slip system pairings. This observation challenges existing models which base dislocation multiplication and strain hardening due to formation of dislocation networks on slip-system-wise approaches in which other slip systems only contribute to a single dislocation spacing. In contrast, the proposed model is based on the coupling of slip systems by dislocation reactions, resulting in an interplay between dislocation

multiplication and limitation of dislocation expansion. This leads to an average density evolution as well as a local density distribution which is very close to DDD simulations. Here, mobile dislocations are generated due to cross-slip or glissile reactions, which leads to an increase in line length and thus decreases the dislocation spacings in the network. The consequence is a formation of a dislocation network consisting of stable dislocation structures with a range of critical stresses to unzip sessile junctions.

This work provides a physically based extension of the CDD framework by incorporating mechanisms which determine the characteristics of dislocation networks by separating dislocation expansion from the slip-system-coupling mechanisms.

Acknowledgements

This work was performed on the computational resource ForHLR II funded by the Ministry of Science, Research and the Arts Baden-Wuerttemberg and DFG ("Deutsche Forschungsgemeinschaft"). The Financial support for the research group FOR1650 Dislocation based Plasticity funded by the German Research Foundation (DFG) under the contract numbers GU367/36-2 and WE3544/5-2 as well as the support by the European Social Fund (Wrangell-Program) and the Ministry of Science, Research and the Arts Baden-Wuerttemberg (Az: 33-7533.-9-10/20/1) is gratefully acknowledged.

Appendix A. Extended results for the nonlocal simulation.

In this Appendix, we investigate the evolution of the averaged dislocation density in the nonlocal CDD simulation using the system setup and parameters explained in section 3.3.2. The total dislocation density per slip system over strain is shown in Fig. A.1(a). The dislocation density increases on active and inactive slip systems in accordance with the DDD results. However, the increase is slightly nonlinear on active and inactive slip systems after about 0.5 % strain and a small rise in dislocation density after overcoming the yield stress is observed. Nonetheless, the fractional distribution of the involved dislocation densities (mobile ρ_{M}, Lomer ρ_{Lomer} and stabilized dislocation density ρ_{S}) summarized over all slip systems shows a relatively uniform profile throughout the simulation after an initial mobilization phase of the dislocation network, shown in Fig. A.1(b). The decrease of the fraction of Lomer junctions from around 30 % to below 20 % during the initial phase of the simulation explains the initial rise in dislocation density observed in Fig. A.1(a). This behavior could likely be improved by a more accurate distribution of link lengths, e.g. corresponding to [5].

In order to investigate the cause of the nonlinearity in the evolution of the averaged dislocation density after 0.5 %, we examine the influence of an averaging over different system areas. Unlike the averaging over the full system, as in Fig. A1 or Fig. 11(a), we now consider an averaging of the dislocation density over a central cubic volume with half of the edge length of the full system. This inner volume cuts off the system areas adjacent to open borders and captures about 40 % of the Gaussian initial dislocation

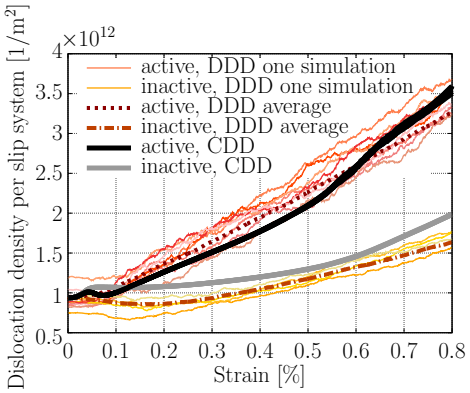

(a) Dislocation density per slip system.

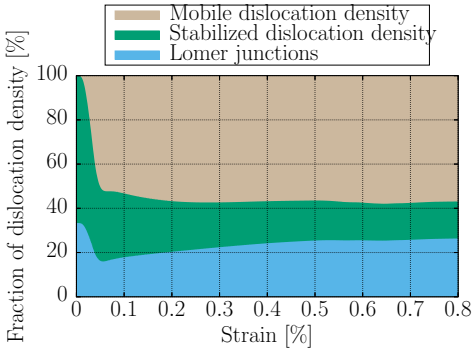

(b) Fraction of dislocation densities (CDD).

Figure A1. As Fig. 11, but for the nonlocal simulation containing dislocation fluxes.

distribution despite having a significantly smaller volume fraction. Fig. A2 shows the average density evolution in this inner system area compared to the CDD results in Fig. A.1(a) relative to the respective initial densities. Compared to the average over the full system, the relative density increase in the system center is almost linear. This confirms that the observed nonlinearity is caused by density in system areas outside the center, i.e. in areas which contain relatively low dislocation density, but still contribute significantly to the *total* density due to the high volume fraction. In the underlying DDD simulations, those areas are typically characterized by single, or very few dislocation lines which are likely to behave differently from dislocations in the dense center. However, the continuum model assumes that even at very low dislocation densities a fraction of the density is always involved in reactions, which probably does not sufficiency reproduce the statistical effects at the boundaries.

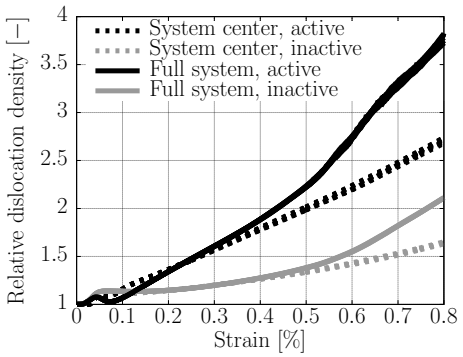

Figure A2. Comparison of the dislocation density per slip system relative to the initial density averaged over the full system (solid lines from Fig. 1(a) normalized with the initial density) and over a central cubic volume with half of the edge length of the full system (dotted lines).

References

[1] J. D. Livingston, "The density and distribution of dislocations in deformed copper crystals," *Acta Metallurgica*, vol. 10, no. 3, pp. 229–239, 1962.

[2] Z. S. Basinski and S. J. Basinski, "Dislocation distributions in deformed copper single crystals," *The Philosophical Magazine: A Journal of Theoretical Experimental and Applied Physics*, vol. 9, no. 97, pp. 51–80, 1964.

[3] C. S. Pande and P. M. Hazzledine, "Dislocation arrays in Cu-Al alloys. I," *The Philosophical Magazine: A Journal of Theoretical Experimental and Applied Physics*, vol. 24, no. 191, pp. 1039–1057, 1971.

[4] M. Stricker, M. Sudmanns, K. Schulz, T. Hochrainer, and D. Weygand, "Dislocation multiplication in stage II deformation of fcc multi-slip single crystals," *Journal of the Mechanics and Physics of Solids*, vol. 119, pp. 319–333, 2018.

[5] R. B. Sills, N. Bertin, A. Aghaei, and W. Cai, "Dislocation Networks and the Microstructural Origin of Strain Hardening," *Physical Review Letters*, vol. 121, no. 8, p. 085501, 2018.

[6] L. Kubin, B. Devincre, and T. Hoc, "Modeling dislocation storage rates and mean free paths in face-centered cubic crystals," *Acta Materialia*, vol. 56, no. 20, pp. 6040 – 6049, 2008.

[7] A. Alankar, D. P. Field, and H. M. Zbib, "Explicit incorporation of cross-slip in a dislocation density-based crystal plasticity model," *Philosophical Magazine*, vol. 92, no. 24, pp. 3084–3100, 2012.

[8] U. F. Kocks and H. Mecking, "Physics and phenomenology of strain hardening: The FCC case," *Progress in materials science*, vol. 48, no. 3, pp. 171–273, 2003.

[9] G. I. Taylor, "The Mechanism of Plastic Deformation of Crystals. Part II. Comparison with Observations," *Proceedings of the Royal Society of London. Series A, Containing Papers of a Mathematical and Physical Character*, vol. 145, no. 855, pp. 388–404, 1934.

[10] A. Ma and F. Roters, "A constitutive model for fcc single crystals based on dislocation densities and its application to uniaxial compression of aluminium single crystals," *Acta Materialia*, vol. 52, no. 12, pp. 3603–3612, 2004.

[11] D. Li, H. Zbib, X. Sun, and M. Khaleel, "Predicting plastic flow and irradiation hardening of iron single crystal with mechanism-based continuum dislocation dynamics," *International Journal of Plasticity*, vol. 52, pp. 3–17, 2014.

[12] H. Leung, P. Leung, B. Cheng, and A. Ngan, "A new dislocation-density-function dynamics scheme for computational crystal plasticity by explicit consideration of dislocation elastic interactions," *International Journal of Plasticity*, vol. 67, pp. 1–25, 2015.

[13] C. Reuber, P. Eisenlohr, F. Roters, and D. Raabe, "Dislocation density distribution around an indent in single-crystalline nickel: Comparing nonlocal crystal plasticity finite-element predictions with experiments," *Acta materialia*, vol. 71, pp. 333–348, 2014.

[14] K. Schulz, M. Sudmanns, and P. Gumbsch, "Dislocation-density based description of the deformation of a composite material," *Modelling and Simulation in Materials Science and Engineering*, vol. 25, no. 6, p. 064003, 2017.

[15] A. Arsenlis and D. M. Parks, "Modeling the evolution of crystallographic dislocation density in crystal plasticity," *Journal of the Mechanics and Physics of Solids*, vol. 50, no. 9, pp. 1979–2009, 2002.

[16] R. Madec, B. Devincre, L. Kubin, T. Hoc, and D. Rodney, "The Role of Collinear Interaction in Dislocation-Induced Hardening," *Science*, vol. 301, no. 5641, pp. 1879–1882, 2003.

[17] B. Devincre, L. Kubin, and T. Hoc, "Physical analyses of crystal plasticity by {DD} simulations," *Scripta Materialia*, vol. 54, no. 5, pp. 741 – 746, 2006.

[18] T. Hochrainer, S. Sandfeld, M. Zaiser, and P. Gumbsch, "Continuum dislocation dynamics: Towards a physical theory of crystal plasticity," *Journal of the Mechanics and Physics of Solids*, vol. 63, pp. 167 – 178, 2014.

[19] T. Hochrainer, "Multipole expansion of continuum dislocations dynamics in terms of alignment

tensors," *Philosophical Magazine*, vol. 95, no. 12, pp. 1321–1367, 2015.

[20] K. Schulz, L. Wagner, and C. Wieners, "A mesoscale continuum approach of dislocation dynamics and the approximation by a Runge-Kutta discontinuous Galerkin method," *International Journal of Plasticity*, 2019.

[21] M. Sudmanns, M. Stricker, D. Weygand, T. Hochrainer, and K. Schulz, "Dislocation multiplication by cross-slip and glissile reaction in a dislocation based continuum formulation of crystal plasticity," *Journal of the Mechanics and Physics of Solids*, vol. 132, p. 103695, 2019.

[22] S. Schmitt, P. Gumbsch, and K. Schulz, "Internal stresses in a homogenized representation of dislocation microstructures," *Journal of the Mechanics and Physics of Solids*, vol. 84, pp. 528–544, 2015.

[23] G. James, D. Witten, T. Hastie, and R. Tibshirani, *An Introduction to Statistical Learning*. Springer New York, 2013.

[24] C. Wieners, "A geometric data structure for parallel finite elements and the application to multigrid methods with block smoothing," *Computing and Visualization in Science*, vol. 13, no. 4, pp. 161–175, 2010.

[25] C. Wieners, "Distributed Point Objects. A New Concept for Parallel Finite Elements," in *Domain Decomposition Methods in Science and Engineering* (T. J. Barth, M. Griebel, D. E. Keyes, R. M. Nieminen, D. Roose, T. Schlick, R. Kornhuber, R. Hoppe, J. Périaux, O. Pironneau, O. Widlund, and J. Xu, eds.), vol. 40, pp. 175–182, Berlin/Heidelberg: Springer-Verlag, 2005.

[26] L. Kubin, *Dislocations, mesoscale simulations and plastic flow*, vol. 5. Oxford University Press, 2013.

[27] R. Madec, B. Devincre, and L. Kubin, "From dislocation junctions to forest hardening," *Physical review letters*, vol. 89, no. 25, p. 255508, 2002.

[28] R. Lagneborg and B.-H. Forsen, "A model based on dislocation distributions for work-hardening and the density of mobile and immobile dislocations during plastic flow," *Acta Metallurgica*, vol. 21, no. 6, pp. 781–790, 1973.

[29] J. A. El-Awady, M. Wen, and N. M. Ghoniem, "The role of the weakest-link mechanism in controlling the plasticity of micropillars," *Journal of the Mechanics and Physics of Solids*, vol. 57, no. 1, pp. 32–50, 2009.

[30] P. Franciosi, M. Berveiller, and A. Zaoui, "Latent hardening in copper and aluminium single crystals," *Acta Metallurgica*, vol. 28, no. 3, pp. 273–283, 1980.

[31] M. Stricker and D. Weygand, "Dislocation multiplication mechanisms – Glissile junctions and their role on the plastic deformation at the microscale," *Acta Materialia*, vol. 99, no. Supplement C, pp. 130–139, 2015.

[32] F. Roters, M. Diehl, P. Shanthraj, P. Eisenlohr, C. Reuber, S. Wong, T. Maiti, A. Ebrahimi, T. Hochrainer, H. Fabritius, and others, "DAMASK - The Duesseldorf advanced material simulation Kit for modelling multi-physics crystal plasticity, damage, and thermal phenomena from the single crystal up to the component scale," *Comput. Mater. Sci*, 2018.

[33] D. Rodney and R. Phillips, "Structure and Strength of Dislocation Junctions: An Atomic Level Analysis," *Phys. Rev. Lett.*, vol. 82, no. 8, pp. 1704–1707, 1999.

[34] C. S. Shin, M. C. Fivel, D. Rodney, R. Phillips, V. B. Shenoy, and L. Dupuy, "Formation and strength of dislocation junctions in FCC metals : A study by dislocation dynamics and atomistic simulations," *J. Phys. IV France*, vol. 11, no. PR5, pp. Pr5–19–Pr5–26, 2001.

[35] G. Schoeck and R. Frydman, "The Contribution of the Dislocation Forest to the Flow Stress," *physica status solidi (b)*, vol. 53, no. 2, pp. 661–673, 1972.

[36] V. B. Shenoy, R. V. Kukta, and R. Phillips, "Mesoscopic Analysis of Structure and Strength of Dislocation Junctions in fcc Metals," *Phys. Rev. Lett.*, vol. 84, no. 7, pp. 1491–1494, 2000.

[37] A. Alankar, I. N. Mastorakos, D. P. Field, and H. M. Zbib, "Determination of Dislocation Interaction Strengths Using Discrete Dislocation Dynamics of Curved Dislocations," *Journal of Engineering Materials and Technology*, vol. 134, no. 2, pp. 021018–021018–4, 2012.

[38] M. Sudmanns, P. Gumbsch, and K. Schulz, "Plastic flow and dislocation strengthening in a

dislocation density based formulation of plasticity," *Computational Materials Science*, vol. 151, pp. 317–327, 2018.